NASA Contractor Report 181792

Experimental Assessment of Helicopter Rotor Turbulence Ingestion Noise in Hover

J. C. Simonich, R. H. Schlinker, and R. K. Amiet

United Technologies Research Center
East Hartford, CT

Contract NAS1-17763

June 1989

National Aeronautics and
Space Administration

Langley Research Center
Hampton, Virginia 23665-5225

CONTENTS

LIST OF FIGURES

LIST OF TABLES

SUMMARY

A model helicopter rotor was tested in an anechoic chamber in hover in a closed chamber so that turbulence generated by the rotor was reingested by the recirculating flow into the rotor. An analytical procedure was developed to use measured aerodynamic properties at the rotor to predict the noise due to turbulence ingestion. The noise generation model is based on an analysis and computer code previously developed by Amiet for non-isotropic turbulence.

The experiment confirmed that the turbulence at the rotor was non-isotropic. Integral length scales computed from measured auto and cross correlations determined that typical eddies were 30 times longer than they were wide. Measured power spectra were similar to isotropic von Karman spectra but offset in amplitude, indicating a degree of non-isotropy.

The measured noise spectrum showed quasi-tonal noise out to at least 20 harmonics, before changing to broadband in character. The polar directivity of the measured noise spectrum peaks at about 20° off the rotor axis and falls to a minimum in the plane of the rotor for the 5th through the 14th harmonics. The noise level at the blade passage frequency increases as the polar angle approaches the rotor plane. Increasing blade pitch angle and blade tip speed increases the measured sound pressure level for all measured tip speeds.

The prediction procedure which was devised can be used to reasonably calculate absolute sound pressure levels for the quasi–tonal and broadband spectrum generated by non–isotropic turbulence ingestion. Five rotor aerodynamic input parameters are needed: axial inflow velocity, radial velocity, axial turbulence integral length scale, radial integral length scale, and turbulence intensity.

The predictive procedure was found to be primarily sensitive to three inputs: turbulence intensity, and the two length scales. The sensitivity of the length scales was confined mainly to high frequencies, while changes to the turbulence intensity affected the entire spectrum. A change in turbulence intensity from 2.25% to 10% increased the predicted sound pressure level by 12 dB.

The general agreement between the noise prediction theory and the experiment was good, although the theory overpredicts the quasi-tonal noise in the low to mid range frequencies and underpredicts the higher frequency broadband signals. The measured polar directivity trends were matched by the predictions for low to mid harmonics, except in the plane of the rotor. At this angle, other noise generation mechanisms are more important, such as unsteady thickness noise. Since the analysis was developed for unsteady inflow noise generation, the steady loading blade passage frequency was not predicted.

INTRODUCTION

Turbulence ingestion is a quasi–tonal and broadband noise mechanism which can contribute to the rotor noise of a helicopter in hover. It occurs when a turbulent eddy is ingested into a rotor blade and chopped. Due to the high contraction ratio during hover, the turbulent eddies are typically stretched into an elongated shape, resulting in non-isotropic turbulence interactions with the blades. When the eddies are non-isotropic, they tend to be much longer than they are wide. The large, elongated eddies are chopped a multiple number of times and contribute the quasi-harmonic tones in the low to mid frequencies. Eddies of smaller scale are only chopped by a single blade and lead to high frequency broadband noise.

The turbulence ingestion noise problem has been investigated experimentally and analytically at UTRC for over a decade. First, interactions of isotropic turbulence with an isolated airfoil were examined. Later, the case of a rotating blade with isotropic turbulence was treated, including a comparison between theory and experiment. More analytical studies at UTRC performed rigorous calculations of the sound produced by a stretched eddy, as well as modeled the details of the stretching process. The current study provides a benchmark experiment with a rotating blade interacting with non-isotropic turbulence to compare with the theory.

LIST OF SYMBOLS AND NOMENCLATURE

ℓ_1	Longitudinal or streamwise integral length scale
ℓ_2	Lateral or cross stream integral length scale
ℓ_1^y	Transverse integral length scale
r_x	Displacement in x direction
R_{ij}	Velocity correlation function
$\tilde{R}_{ij}$	Correlation coefficient
t	Time
T_i^τ	Integral time scale
u	Turbulence velocity fluctuation in the x direction
U	Local time mean velocity
x_i	Upstream Cartesian coordinate system, i=1,2,3
ξ_i	Downstream Cartesian coordinate system, i=1,2,3
τ	Time delay

Subscripts

i,j,k	Specify either a vector or a component of a vector

PREVIOUS INVESTIGATIONS

The concept of turbulence ingestion as a possible noise mechanism is a recent development. A study by Sofrin and McCann[1] in 1966 indicated that ingestion of turbulence might be a possible source of rotating blade harmonic noise. The first conclusive experimental evidence was obtained by Hanson[2] in 1974. He determined that spectral peaks from propellers, helicopter rotors and fans were probably due to ingestion of atmospheric turbulence and not due to fixed inflow distortion as had previously been assumed.

Paterson and Amiet[3] performed an experiment in 1979 to study the effect of turbulence ingestion on the noise generated by a model helicopter rotor. They used both grid generated turbulence in a wind tunnel as well as naturally occuring atmospheric turbulence. The grid generated turbulence was nearly isotropic a short distance downstream of the grid. Test conditions included forward flight and vertical ascent. They were unable to generate turbulence from grids which would remain non-isotropic long enough downstream so that it could interact with a rotor. They therefore used naturally occuring non-isotropic turbulence from the atmospheric boundary layer by running their rotor rig outdoors in hover. Both far–field noise spectra and directivity were measured in addition to incident turbulence intensities, length scales and spectra. A theory capable of absolute level prediction of rotor turbulence ingestion noise spectra and directivity was presented. Low frequency narrowband random noise was overpredicted and high frequency broadband noise was underpredicted. However, the existence of this noise source was definitely verified.

PRESENT INVESTIGATION

Objectives

The overall objective of the present study was to provide an experimental assessment of the accuracy of a turbulence ingestion noise theory for a helicopter rotor developed by Amiet[4]. An exact test of the theory which is capable of handling non–isotropic turbulence would require the complete description of the flow into the rotors. This experiment provided data to validate the theory for non-isotropic turbulence. Representative measurements of the flow into the rotor were acquired in the present study. Simultaneous far–field noise and rotor inflow turbulence statistics were acquired.

The particular nature of the turbulence ingestion mechanism is illustrated in Figure 1. In this test, a hovering rotor in a closed chamber was used so that turbulence generated

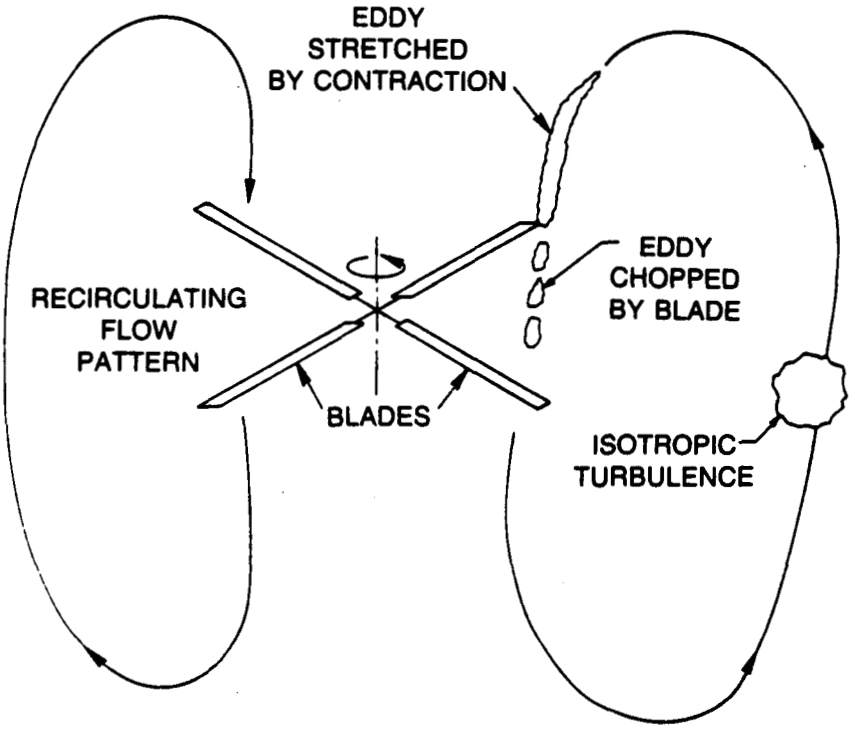

Figure 1: Turbulence Ingestion Noise Mechanism

by the rotor was reingested by the recirculating flow into the rotor. In this manner, a non-isotropic turbulent eddy generated by the blades is allowed to relax to more nearly isotropic conditions before being contracted by the rotor inflow and stretched into a non-isotropic eddy. It is this non-isotropic eddy that interacts with the blade and generates the noise. Although ingestion of isotropic turbulence also causes noise (see reference [4]), it is more common for helicopter in hover to interact with non-isotropic turbulence. A non-isotropic eddy which is stretched into an elongated shape by the contraction effect of a hovering rotor will be chopped a multiple number of times, which results in harmonics appearing at much higher frequencies than steady loading noise would create.

Approach

A model helicopter main rotor was tested in an anechoic chamber. Non-isotropic turbulence was ingested by the rotor by recirculating the rotor–generated turbulence. The high contraction ratio of the rotor in hover accounted for the large stretching of the turbulence at the rotor face. Inflow turbulence self and cross product statistics were acquired at a number of locations a small distance above the rotor simultaneously with noise data. Rotor tip Mach number and pitch were varied to see the effect on noise.

DESCRIPTION OF THE EXPERIMENT

Acoustic Research Tunnel

This study was conducted at the UTRC Acoustic Research Tunnel. Although the tunnel has forward flight capability, this capability was not utilized in the current experiment since the rotor was only operated in hover inside the anechoic chamber. (The facility is described in detail by Paterson[5].) The chamber is 4.9 m (16 ft) high, 5.5 m (18 ft) long (in the rotor axis direction) and 6.7 m (22 ft) wide. The chamber walls are lined with 0.5 m (1.5 ft) high fiberglass acoustic wedges which provide an anechoic environment above 175 Hz. The inlet to the chamber and the collector were sealed and covered with acoustic foam to prevent air drafts and eliminate any reflecting surfaces.

Experimental Arrangement

Figures 2, 3, and 4 show photographs of the anechoic chamber experimental arrangement. A four bladed rotor of 0.76 m (28 in) dia with untwisted NACA 0012 blades of 5.1 cm (2 in) chord with rectangular planform was used. The blade pitch angle was set with a blade profile template and an inclinometer. Rotor rotational speed was set by the use of a variable frequency control. The speed was monitored using a once- per-revolution pulse generated by an optical sensor. This pip signal was also recorded on analog tape. A Hama[6] trip strip of the type used by Schlinker and Amiet[7] was used on the blades to trip the boundary layer. This was done to force the boundary layer on the blades to become turbulent and eliminate the laminar boundary layer vortex shedding noise mechanism. The technique used consisted of cutting a strip of adhesive backed aluminum tape with pinking shears to produce a uniformly jagged edge and then attaching the tape to both the pressure and the suction surfaces of the blades.

The test rig was powered by a 150 HP variable frequency drive motor. The rotor was rotated in a vertical plane so that ground mounted microphones could be utilized. The rig was mounted on a frame so that the centerline of the rotor was half way between the ceiling and the floor of the chamber. The rig was positioned 3 m (9 ft) from the acoustic wedges on the thrust direction wall and 2 m (6 ft) from the wedges on the downwash wall so that microphones could be positioned in the acoustic far–field.

Ten microphones in a fixed array on a 1.83 m (6 ft) radius arc were centered on the rotor hub. The microphones were located in a horizontal plane at the rotor hub height at 10° increments between 0° and 90° from the rotor axis. A schematic of the microphone arrangement is shown in Figure 5.

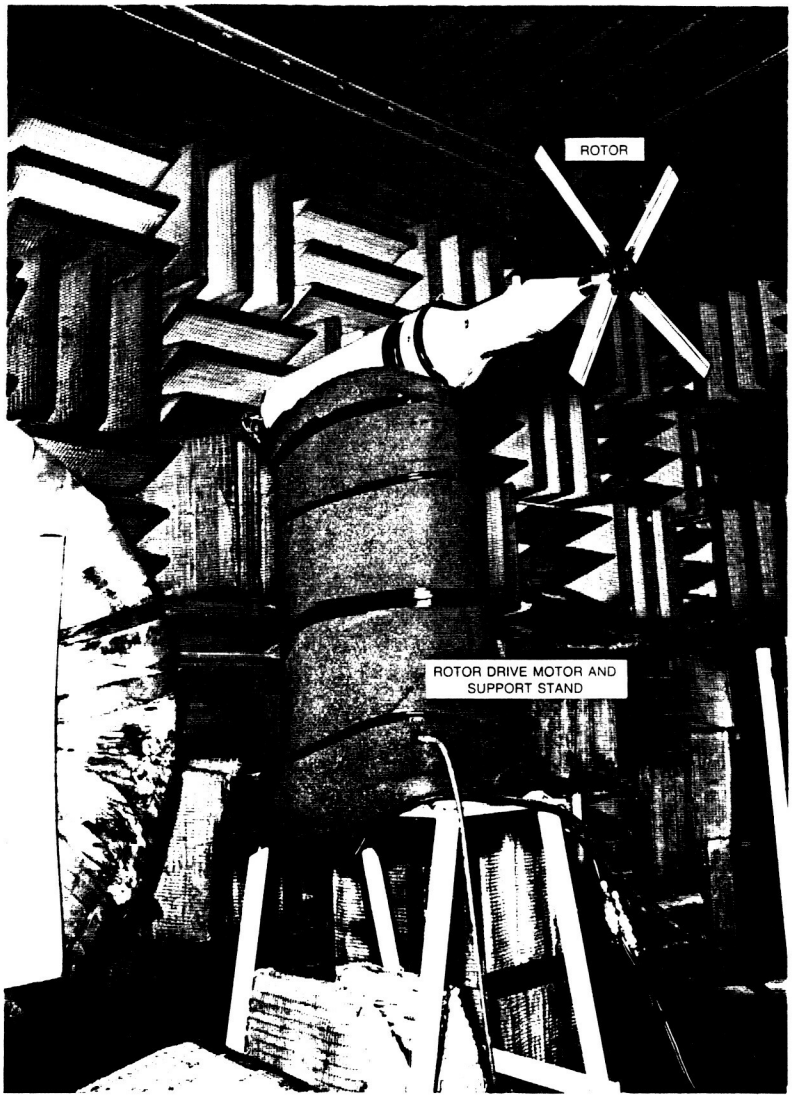

Figure 2: Rotor Drive Rig in Anechoic Chamber

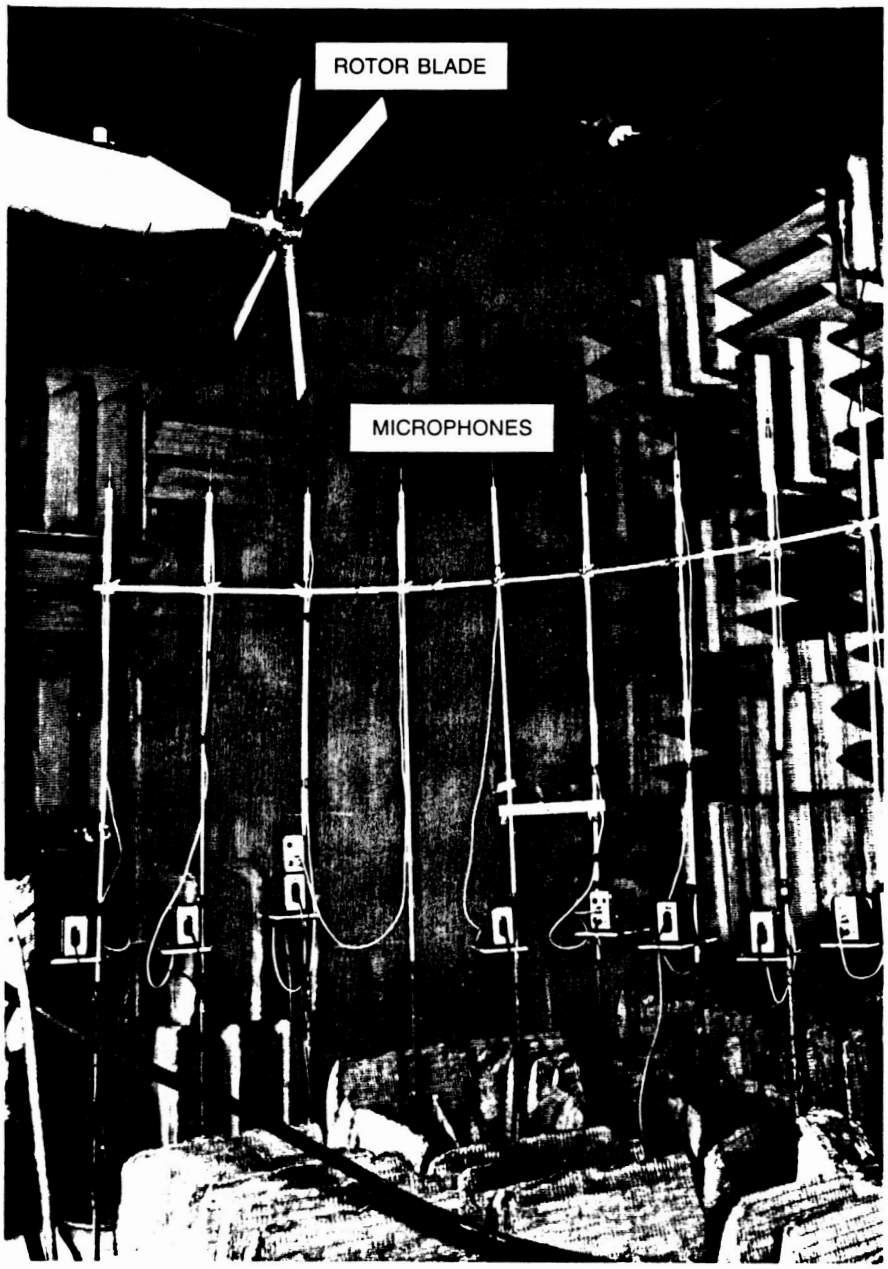

Figure 3: Rotor Drive Rig and Microphones in Anechoic Chamber

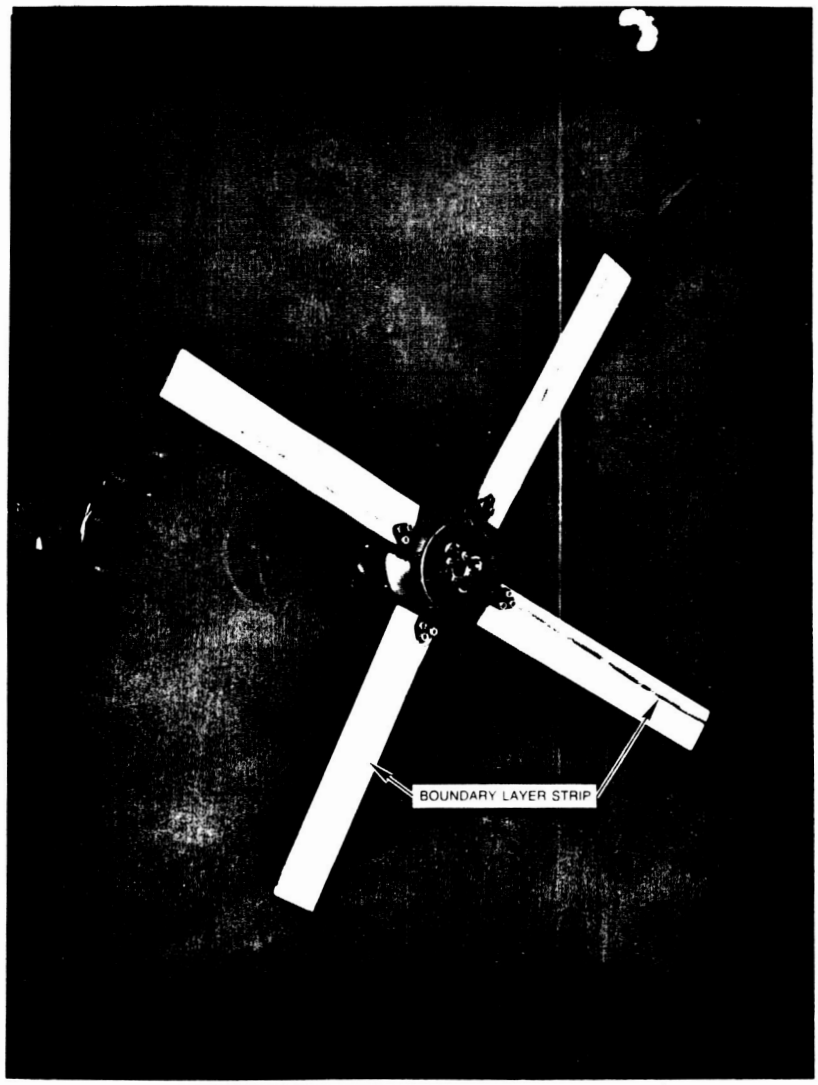

Figure 4: Closeup of Rotor Showing Hama Trips

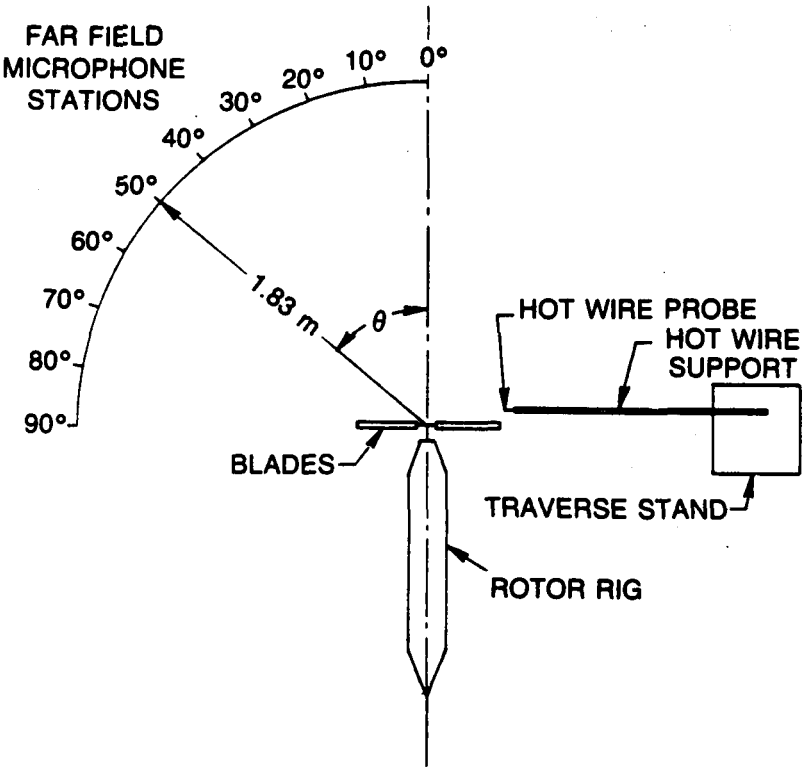

Figure 5: Overhead View of Microphone and Hot Film Arrangement in Anechoic Chamber

The rotor inflow was measured with two pairs of cross hot film probes, one fixed and one remotely movable. In order to avoid altering the flow characteristics, the two axis traverse stand was left in the same location regardless of the measurement location and was covered with acoustic foam to avoid reflections. The geometry used in the experiment is shown in Figure 6.

The inflow into the rotor was visualized using a smoke probe technique. This was used for diognostic purposes to search for asymmetry in the flow as well as to trace inflow particle lines.

Instrumentation

Acoustic Measurements — A sketch of the acoustic instrumentation system is shown in Figure 7. Measurements of the far field noise were made with 0.635 cm (0.25 in) diameter condenser microphones at grazing incidence. (Grazing was chosen over normal incidence since it provides a flatter frequency response out to high frequency.) The frequency response of these microphones was flat for the range of interest in this study (120 to 20,000 Hz). The microphone preamplifier signals were amplified and recorded on magnetic tape,

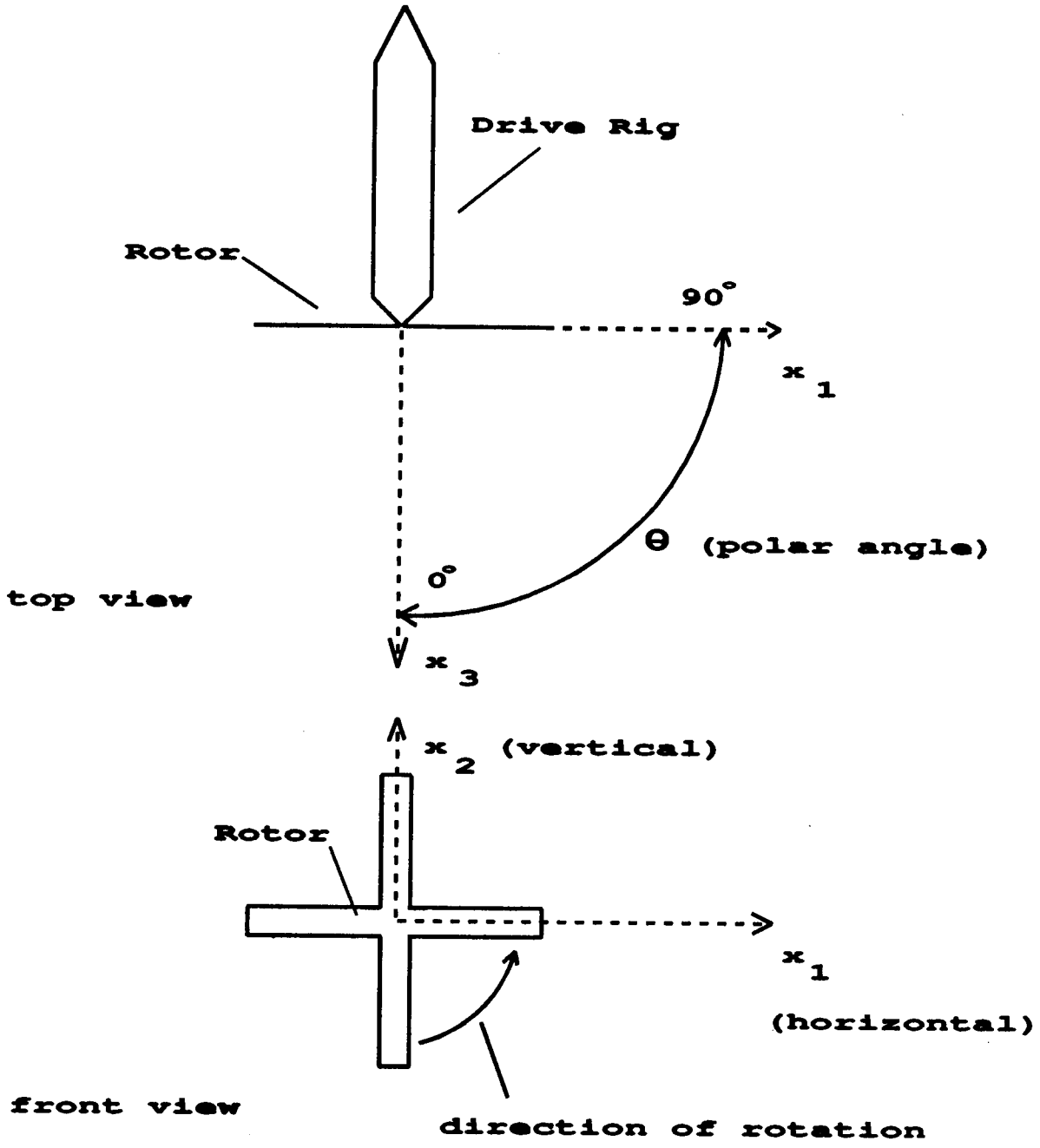

Figure 6: Geometry and Coordinate System for Experiment

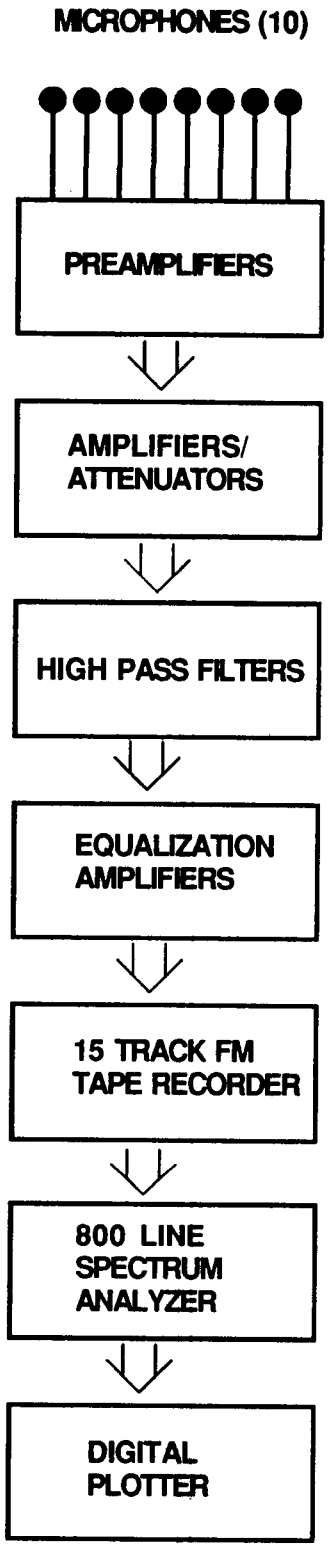

Figure 7: Acoustic Instrumentation System

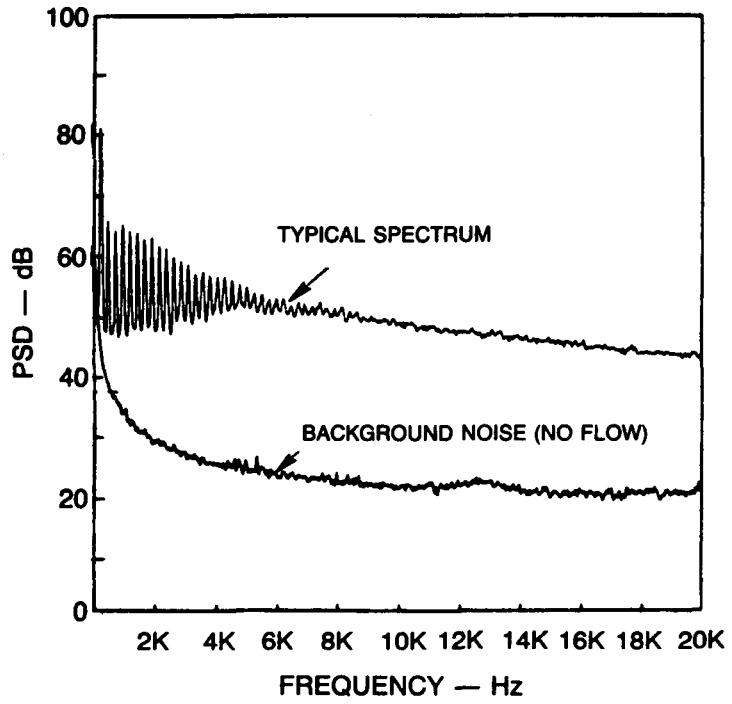

Figure 8: Background Noise Level

using a 14 track, FM tape recorder system in wide band group II at 30 ips, giving a maximum frequency response of 125 kHz. Data were typically averaged 200 times. Acoustic data were reduced to narrow band spectra on an 800 line spectrum analyzer. The effective bandwidth was 25 Hz for the 0–20 kHz range typically used, and other ranges can be determined by direct proportion. Hardcopy plots were produced. Since no direct digital transfer method between the analyzer and the laboratory computer was available, these plots were later digitized for analysis and comparison to predicted noise levels.

Signal attenuation due to atmospheric attenuation was not accounted for in the data reduction due to the low frequencies (maximum of 20 kHz) and small sound propagation distances in the current experiment.

A comparison between background noise levels and a typical turbulence noise spectrum is shown in Figure 8. The background noise data were recorded without the rig running and represents ambient chamber noise levels. The measured signal-to-noise ratio is seen to be better than 20 dB for all but the lowest frequencies.

Turbulence Measurements — Turbulence data were acquired using two cross hot film probes. One probe was placed at a fixed location and the other was positioned remotely under computer control. A two axis traversing system was used to move the probe using stepping motors. Traverse increments of 0.0127 mm (0.0005 in) in a closed loop system

were used. The traverse system was moved under computer control and the probe was allowed to stabilize for 10 seconds before taking the measurement. The probe support arm was circular with a flat section welded to the back half to prevent vortex shedding and hence probe vibration. The traversing probe was located 6.4 cm (2.5 in) upstream of the rotor hub. The fixed probe was positioned downstream of the traversing probe by 1.4 cm (9/16 in). Turbulence statistics were assumed to be frozen over the 1.4 cm axial separation distance.

A four channel, linearized, constant temperature anemometer system was used for turbulence measurement. The outputs of the four anemometers were digitized directly by the data acquisition system (discussed in detail in the subsection entitled Data Acquisition System) analog to digital converter (A/D) as well as recorded on FM tape at 7.5 ips. Both the DC coupled signals as well as amplified AC coupled signals from all four hot films were recorded on tape. The encoder position was also stored on the data acquisition system and recorded on FM tape. The raw hot film voltages were then converted to velocity, corrected for temperature changes between run time and calibration and the data were digitally summed and differenced to obtain two orthogonal velocity components. Depending on hot film orientation, these were either axial and radial components or axial and azimuthal components.

Data Acquisition System — Hot film data were acquired in the present study by a computer controlled system. A schematic of the system is shown in Figure 9.

Data acquisition was performed in the following manner. After the rotor operating condition was set and the chamber allowed to come to equilibrium, the data acquisition system was activated. The computer controlled the stepping motor traverse which moved the probe to a preprogrammed point from an array of desired locations. Once the probe reached the requested position (as indicated by an optical encoder) a settling period was taken for the probe to come to equilibrium with its environment. All four hot film sensors were then digitized in sequence as fast as the built in multiplexer could switch channels. This was necessary since a four channel simultaneous sample and hold A/D was unavailable.

Some error is associated with this sequential data acquisition, but it can be shown to be negligible for the sampling rate used in this experiment. A calibration of the error was done. A signal from a sine wave generator was input into channels 1 and 4 (i.e. the channels farthest apart in slew time). The frequency of the generator was varied from 3 Hz to 1000 Hz. The cross correlation coefficient was then calculated for the two channels. The results are shown in Figure 10. As can be seen from the graph, a significant error can be incurred when trying to digitize a signal above 250 Hz. This was not a problem in the current study since the desired sampling frequency was below 30 Hz.

Due to computer memory limitations, only 4,000 points for each hot film channel were

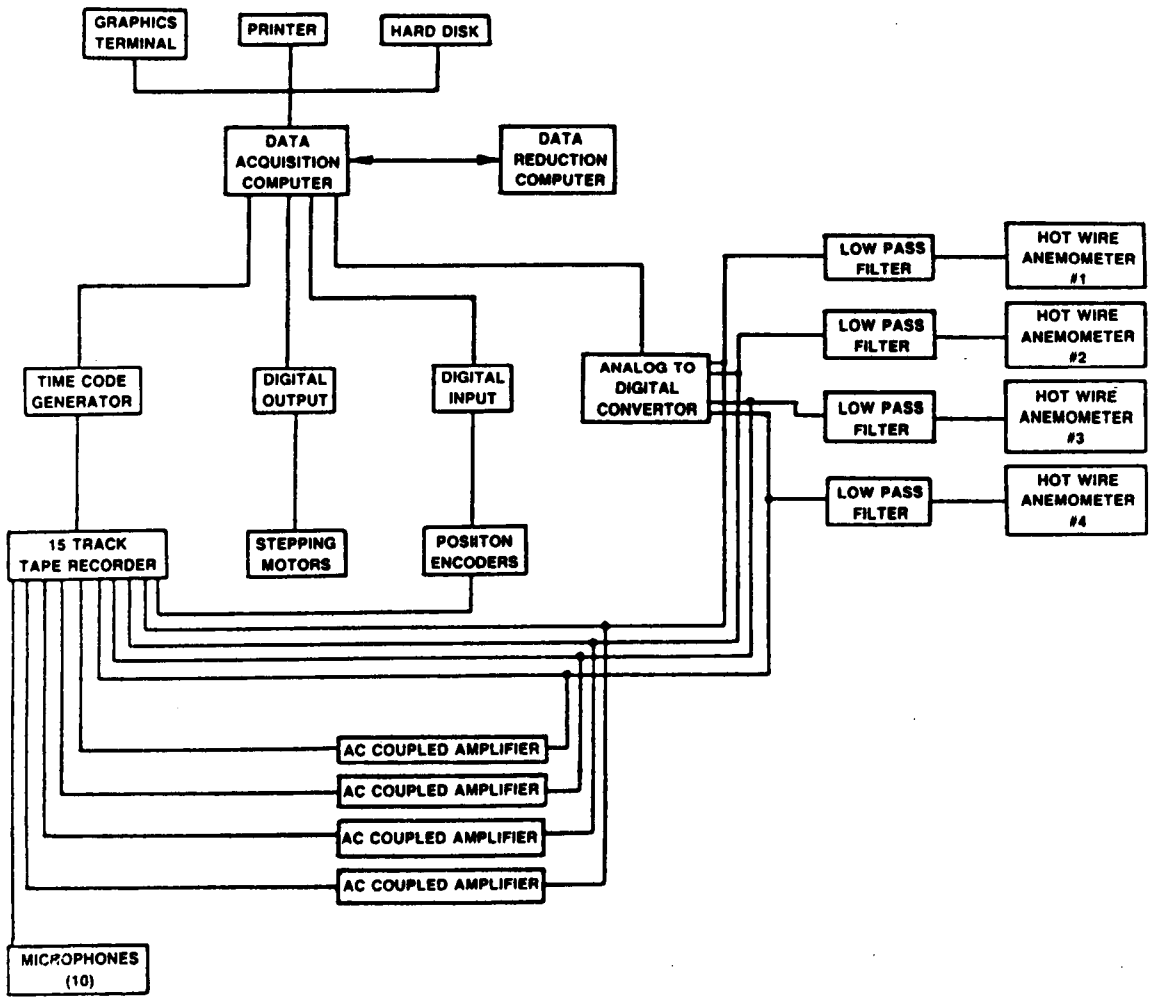

Figure 9: Data Acquisition System

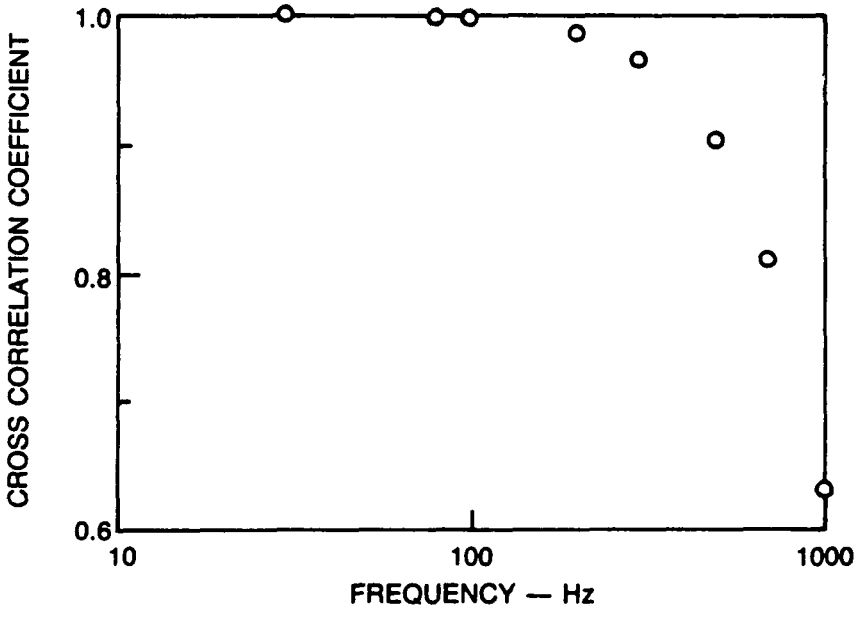

Figure 10: Sequential Channel Digitizing Effect

digitized continuously. Four blocks of 4,000 points taken with a few seconds between them (disk access time) were typically acquired.

The hot film signals were low pass filtered. This was done to prevent the particle velocity of the rotor acoustic near field at shaft and blade passage frequencies from contaminating the inflow turbulence velocity signal. The reason for this was also described by Paterson and Amiet [3]. They showed that inclusion of the blade passage tones resulted in an autocorrelation function which was periodic, making determination of length scales impossible.

The effect of filtering on the power spectrum of the turbulence signal is shown in Figure 11. The signal is virtually unchanged by the filter below the cutoff frequency, but above the cutoff frequency the shaft frequency in the filtered data were reduced by 20 dB and the blade passage frequency were reduced by more than 50 dB.

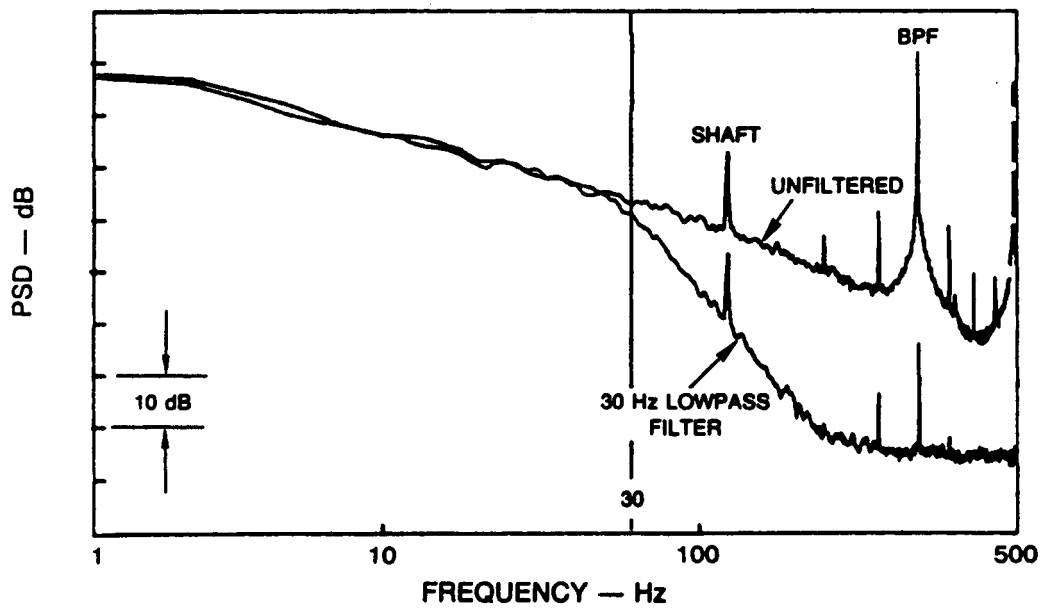

Figure 11: Effect of Lowpass Filtering on Hot Film Data

TEST PROGRAM

The test program is summarized in Table 1. Most of the aerodynamic data was obtained for the 5° pitch angle and 144 m/s tip speed case. It was decided to obtain a comprehensive turbulence statistics measurement set for one operating condition instead of a limited measurement set for many operating conditions, thereby assuring an adequate measurement set for acoustic verification.

FLOW VISUALIZATION

In order to visualize the inflow to the rotor, a smoke probe technique was employed. Smoke was generated at the tip of probe by electrically heating mineral oil. A pumping system feeds oil to the tip and the rate is controllable so that the injection rate matches the local flow velocity. Local heating of the oil is done to avoid condensation of oil if vaporization is carried out further from the point of injection. Figure 12 shows typical results from the flow visualization. This figure shows four particle paths for the rotor at the same operating condition. The turbulent nature of large scale disturbances are clearly

Pitch Angle (degrees)	Tip Speed (m/s)	Acoustic Data	Turbulence Data
5	71.8	•	
5	108	•	
5	144	•	•
5	192	•	P
10	71.8	•	
10	108	•	
10	144	•	
10	192	•	
15	71.8	•	
15	108	•	
15	144	•	P
15	192	•	

P – partial

Table 1: Test Conditions

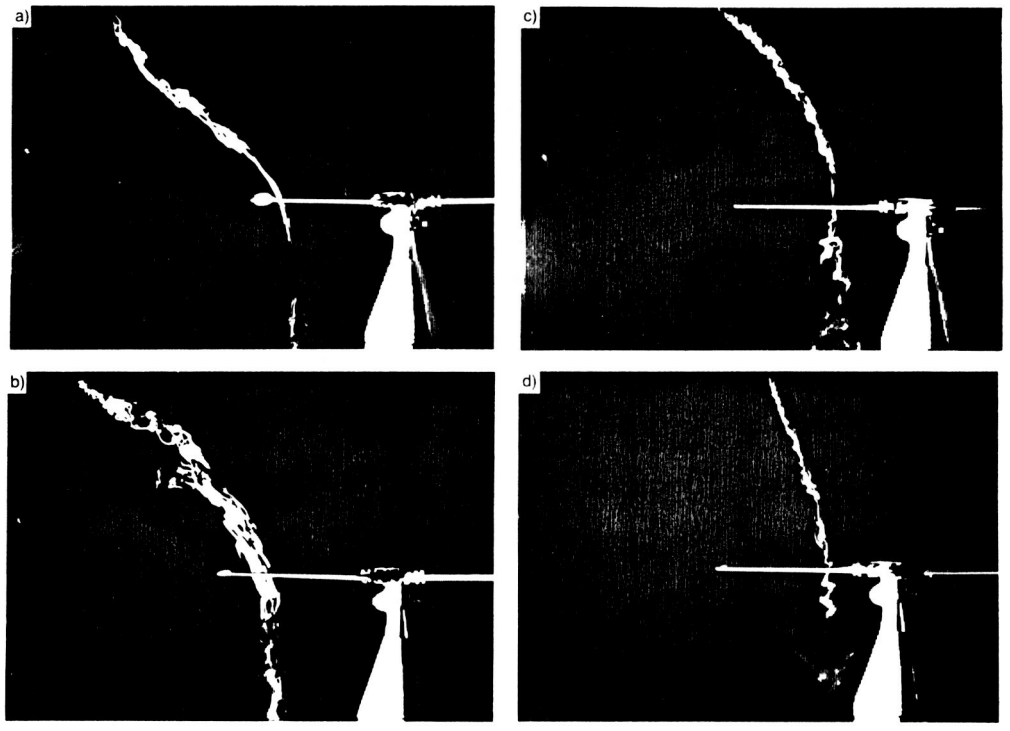

Figure 12: Smoke Flow Visualization of Rotor Inflow

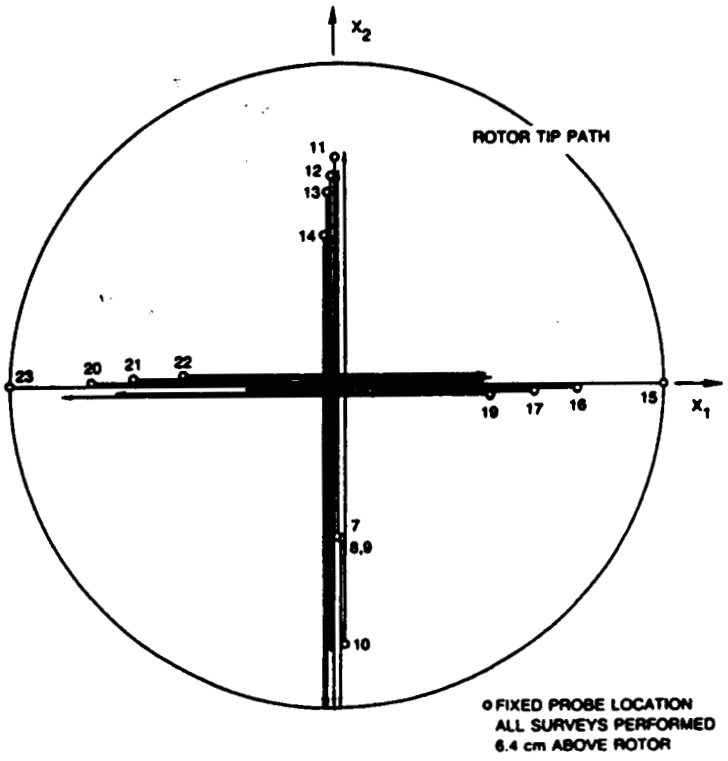

Figure 13: Location of Fixed and Traversing Hot Film Probes

visible in the photos. Near the rotor tip, the streamlines are highly curved, indicating skewing of the turbulent eddies.

ROTOR INFLOW AERODYNAMIC MEASUREMENTS

Data Acquisition and Reduction Procedure

The rotor inflow velocity field was measured using hot film anemometry. Two sets of cross film probes were used, one for a fixed probe and the other for a traversing probe. Hot film data were acquired over both horizontal and vertical traverses. The location of the fixed probe and the traversing probe for each survey is shown in Figure 13.

The data acquisition procedure was as follows: The blade angle was set manually with a blade profile template and an inclinometer. The rig was speed was then set at the required operating condition. The FM tape recorder was then started. Hot film data were then acquired by moving the traversing probe to the desired location, waiting for the probe to

come to equilibrium, and then rapidly filling memory with A/D voltage readings from the four hot film sensors. Once memory was filled, this data set was written in binary format to disk (to increase data transfer rate and conserve disk space), and another block of data was acquired. All individual data points were stored digitally so that the data could be post processed using time series analysis. After several blocks were acquired (typically four blocks of 4000 points), the traversing probe was moved to a new location using the stepping motor driven traverse under computer control. The acquisition process was then repeated until all locations in the scan had been acquired.

Once the 5 Mbyte hard disk was filled, the data set was transferred electronically to a multi-user, 32 bit supermini computer for analysis and reduction. Data reduction was accomplished using a combination of commercially acquired signal analysis software and custom written analysis routines.

Mean Velocity

The mean velocity was obtained by averaging all the data acquired at a given traverse location (typically 16,000 points) for each film sensor. The raw voltages were converted to velocity and corrected for temperature differences between run time and calibration. The velocities for a hot film pair were then summed and differenced digitally to obtain either the axial and radial or axial and tangential data respectively.

The mean, axial velocity profile in front of the rotor plane for the vertical and horizontal traverses respectively is shown in Figure 14. The data obtained in different traverses were consistent and repeatable. However, the flow was slightly different between the horizontal and the vertical traverses and the flow was nonsymmetric. This latter observation was particularly observable in the horizontal data. This asymmetry may be caused by the fact that the room was not perfectly symmetric. The two openings which allow flow to enter and leave the chamber were covered with acoustic foam to eliminate unwanted reflections. Also, the rig was not exactly centered in the room and there was only one hot film traverse stand in the chamber.

Figure 15 shows the mean radial velocity profile measured in front of the rotor plane for vertical and horizontal traverse respectively. The data from several runs were again consistent and repeatable, but again showed nonsymmetry. The radial velocity was seen to reach a negative peak at 95% of the rotor radius.

As a test of the measurement accuracy, several traverses were made to measure the azimuthal component of velocity upstream of the rotor. This should be zero upstream of the rotor since swirl is not introduced into the flow until after the rotor. This plot is shown in Figure 16. As can be seen from the figure, the azimuthal component was found to be

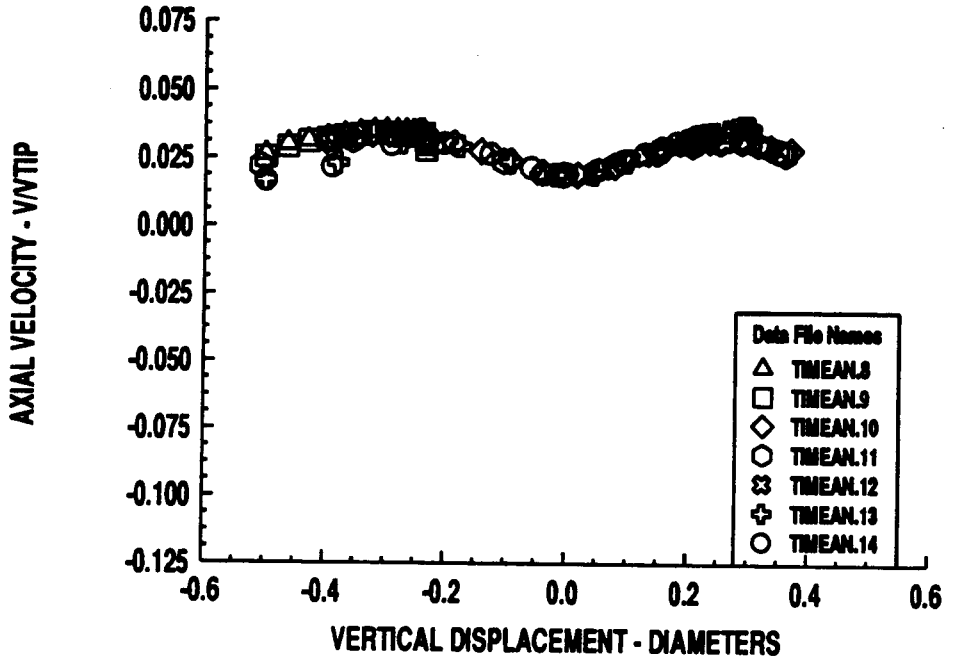

a) Vertical

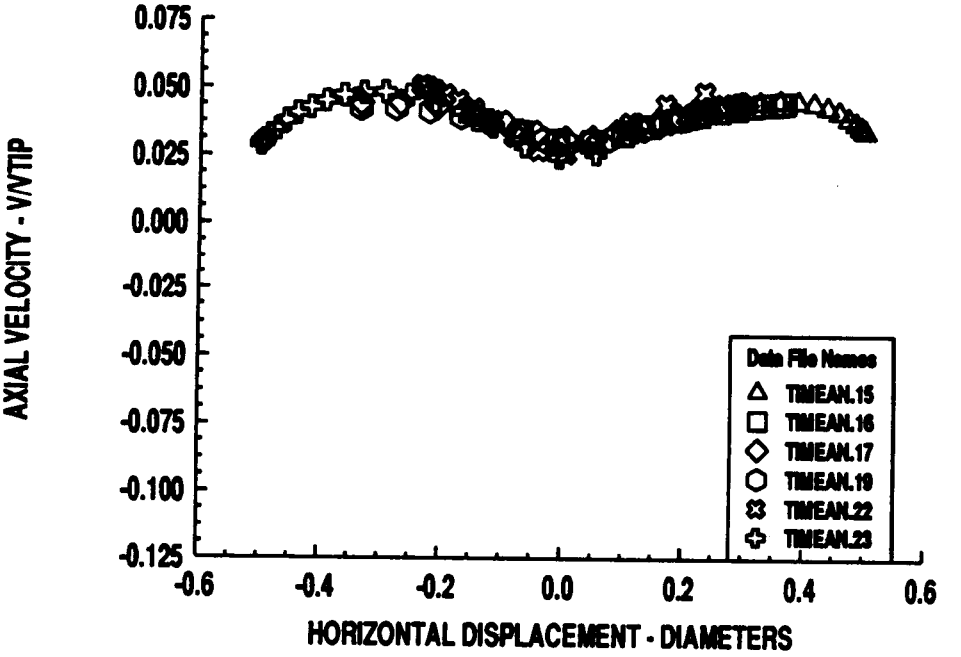

b) Horizontal

Figure 14: Axial Mean Velocity Profiles

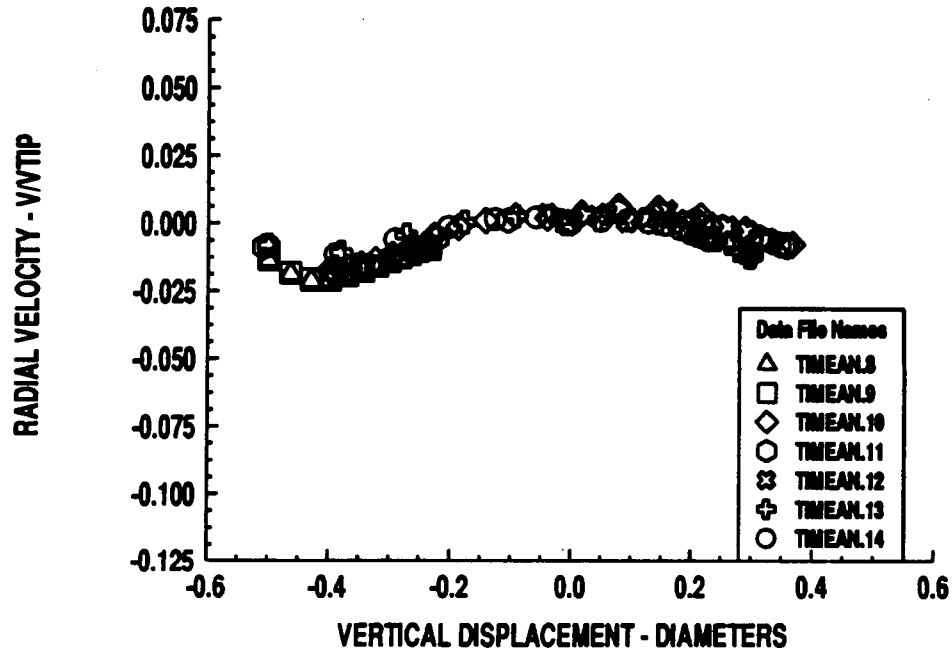

a) Vertical

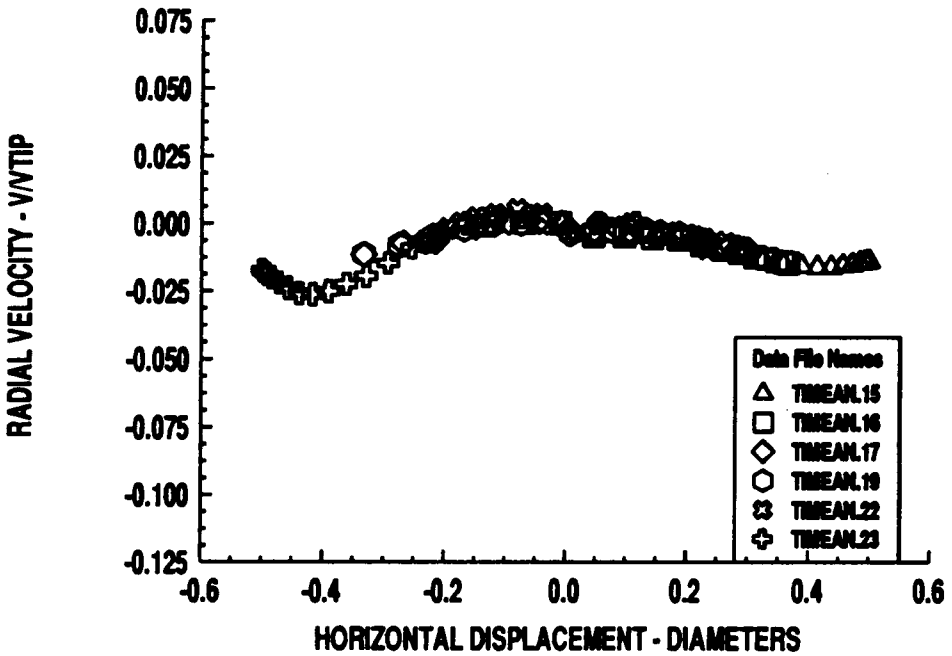

b) Horizontal

Figure 15: Radial Mean Velocity Profiles

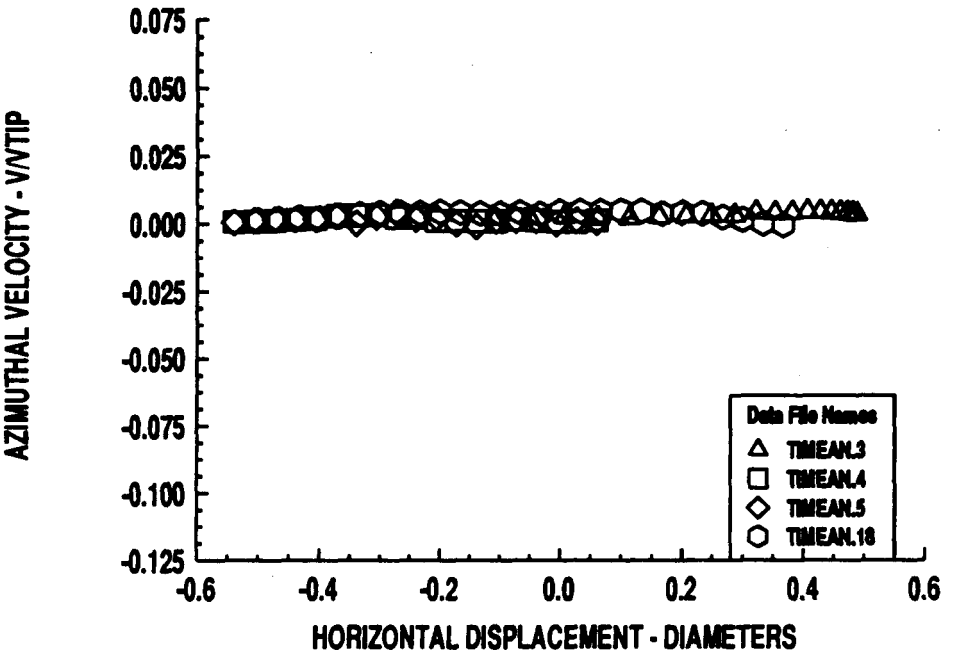

Figure 16: Azimuthal Mean Velocity Profiles

negligible across the rotor.

The variation in the flow magnitude and direction for the vertical and horizontal traverses is shown in Figure 17. In the horizontal survey, the flow does not approach the hub in an axial direction. Rather the flow is skewed as it enters as a result of the asymmetry noted earlier. The results of several surveys are shown on this figure and only a slight variation in magnitude and direction from points taken at nearly the same position is apparent.

RMS Turbulence

The axial component of the rms turbulence intensity normalized by the axial mean velocity as a function of position is shown in Figure 18 for the vertical and horizontal traverses respectively. There is more scatter in these plots than in the mean velocity plots, but the trends are clear. The turbulence intensity is a maximum slightly beyond the rotor tips and dips to a minimum at the 25% radius position. The intensity then increases to a local maximum at the hub. This effect is probably caused by the locally lower axial velocities at the hub.

a) Vertical

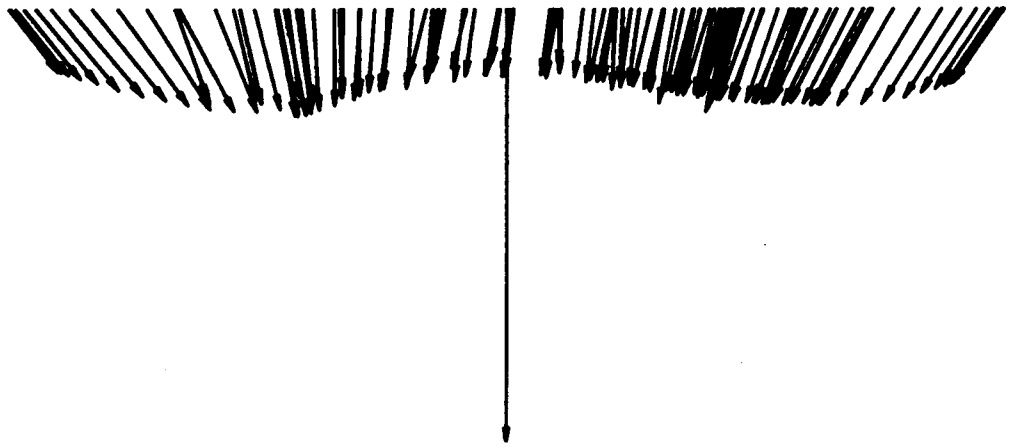

b) Horizontal

Figure 17: Velocity Vector Above Rotor

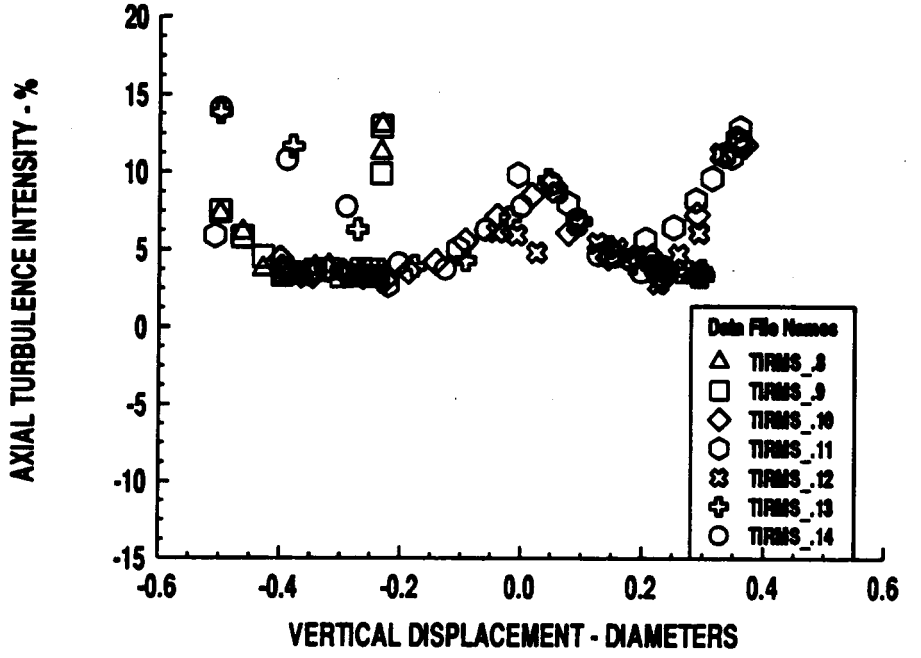

a) Vertical

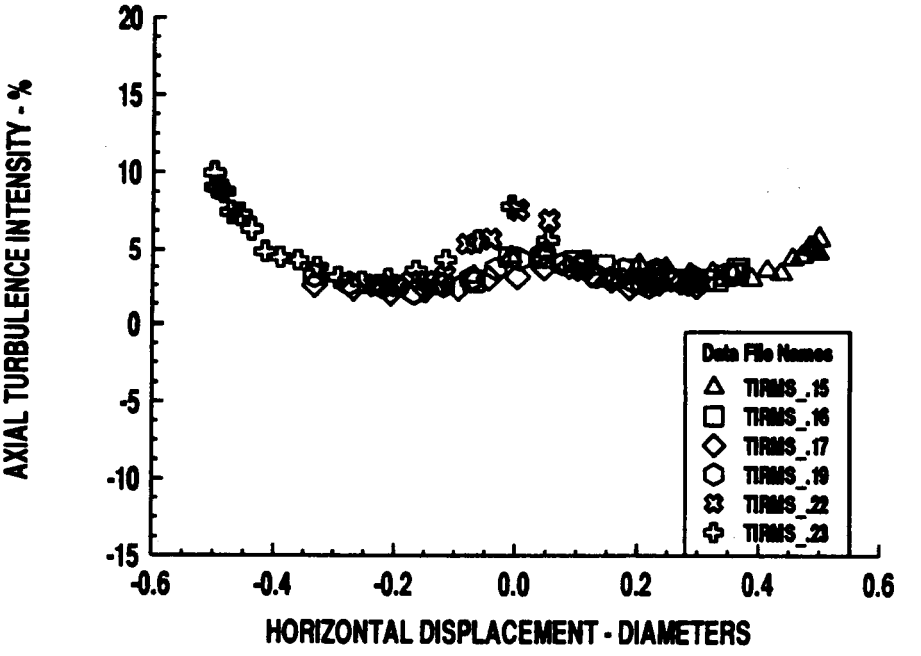

b) Horizontal

Figure 18: Root Mean Square Axial Turbulence Intensity

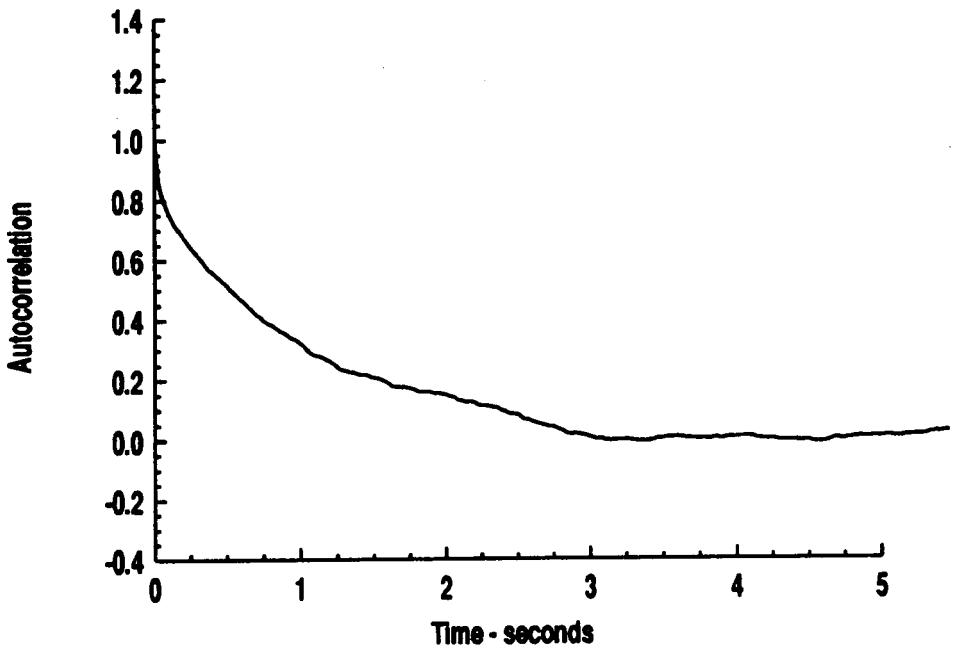

Figure 19: Typical Axial Turbulence Autocorrelation Coefficient

Autocorrelation and Streamwise Integral Length Scale

In order to determine the longitudinal or streamwise integral length scales, the autocorrelation of the signal must first be determined. A typical normalized autocorrelation for the streamwise velocity component is shown in Figure 19. The autocorrelation is unity for a zero time delay and falls off to near zero as the time approaches 3 seconds. The autocorrelations for a typical 20 point survey taken in front of the rotor are shown in an offset plot fashion in Figure 20. As can be seen from the graph, the autocorrelation has the same general shape for all points in the survey. Figure 21 shows another representation of the same data plotted in a contour format. Here, contours of normalized,autocorrelation coefficient are plotted versus position across the rotor face and delay time. For large values of autocorrelation coefficient, there is little variation across the rotor. Lower coefficient contours show some variation across the rotor span, including a decrease near the rotor axis.

The autocorrelation can also be described in terms of a velocity correlation function. A complete set of possible correlations is given by a second order tensor of the form:

$$R_{ij}(\underline{r},\tau) = \overline{u_i(0,0,0,t)u_i(r_x,r_y,r_z,t+\tau)} \qquad (1)$$

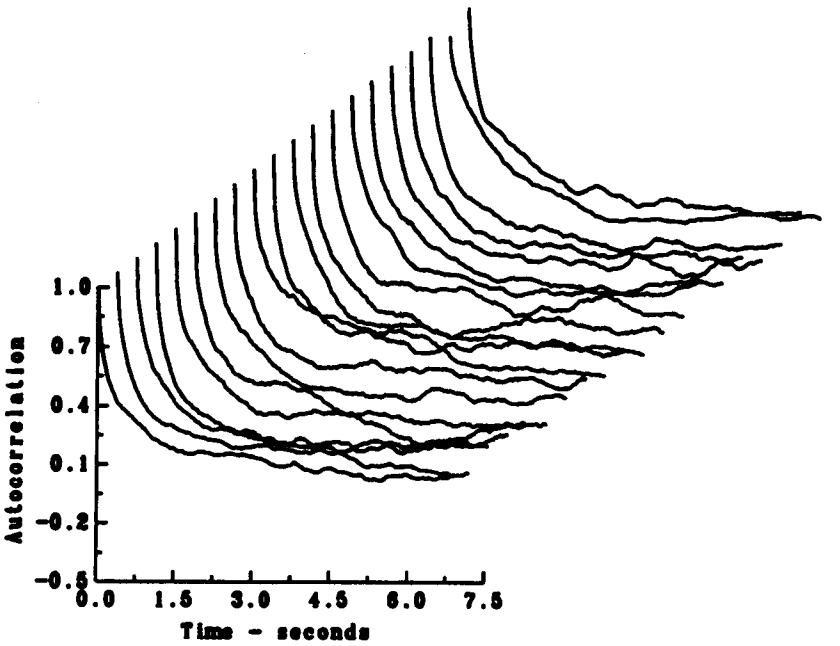

Figure 20: Axial Turbulence Autocorrelation Coefficient Across the Rotor

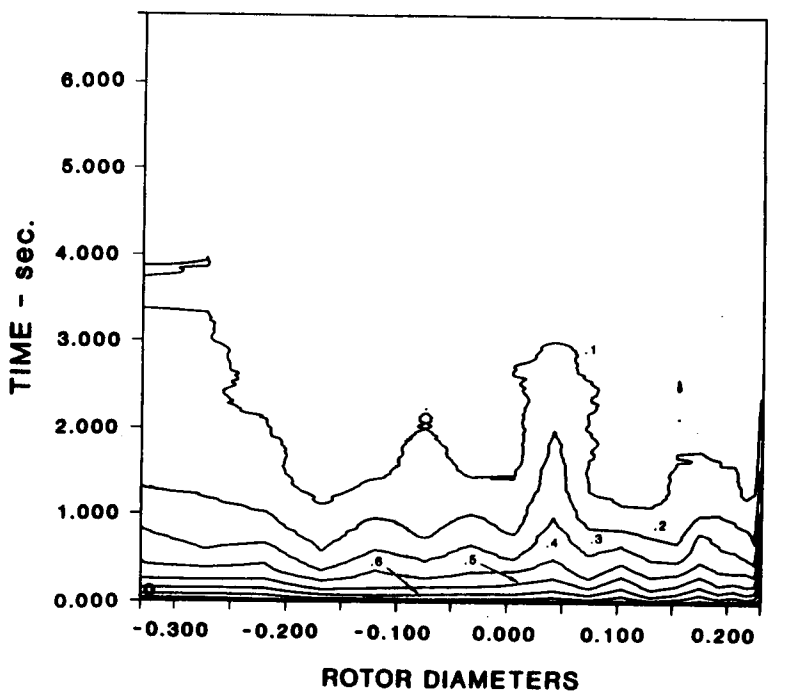

Figure 21: Contours of Autocorrelation in Delay Time and Radial Displacement Space

For the mean, axial velocity, autocorrelation, the particular function of interest is:

$$R_{11}(r_x,0,0,\tau) = \overline{u_1(0,0,0,t)u_1(r_x,0,0,t+\tau)} \tag{2}$$

The correlation functions are generally normalized by using rms values to yield correlation coefficients:

$$\tilde{R}_{11}(r_x,0,0,\tau) = \frac{\overline{u_1(0,0,0,t)u_1(r_x,0,0,t+\tau)}}{\overline{u_1^2}} \tag{3}$$

An integral time scale of the turbulence can be defined by integrating the correlation coefficient:

$$T_i^x = \int_0^\infty \tilde{R}_{11}(\tau)d\tau \tag{4}$$

The axial integral length scale was calculated from the integral time scale by the use of Taylor's frozen flow hypothesis. This hypothesis assumes that the turbulence field is "frozen" as it convects into the measurement probe. This will strictly only hold for homogeneous, isotropic turbulence, but it has been found to be reasonable for other non-isotropic flows. The basic assumption is that:

$$r_x = U\tau \tag{5}$$

Therefore, the integral length scale is related to the integral time scale by:

$$\ell_1^x = \int_0^\infty \tilde{R}_{11}(r_x)dr_x = \int_0^\infty \tilde{R}_{11}(\overline{U}\tau)d\tau = \overline{U}T_i^x \tag{6}$$

In practice, this integral must be evaluated over a finite range. Three different techniques were used to determine the time integral: integration over the complete range of the computed autocorrelation, integration over the autocorrelation until the first non-zero point was reached, or by using the value where the autocorrelation was 1/e of its zero time delay value. The axial integral length scale is shown as a function of measurement location relative to the rotor hub in Figure 22 for the three techniques. There is scatter both between the integration techniques as well as over the range of the traverse. The effect of the variability of the data on the predicted noise output is accessed below.

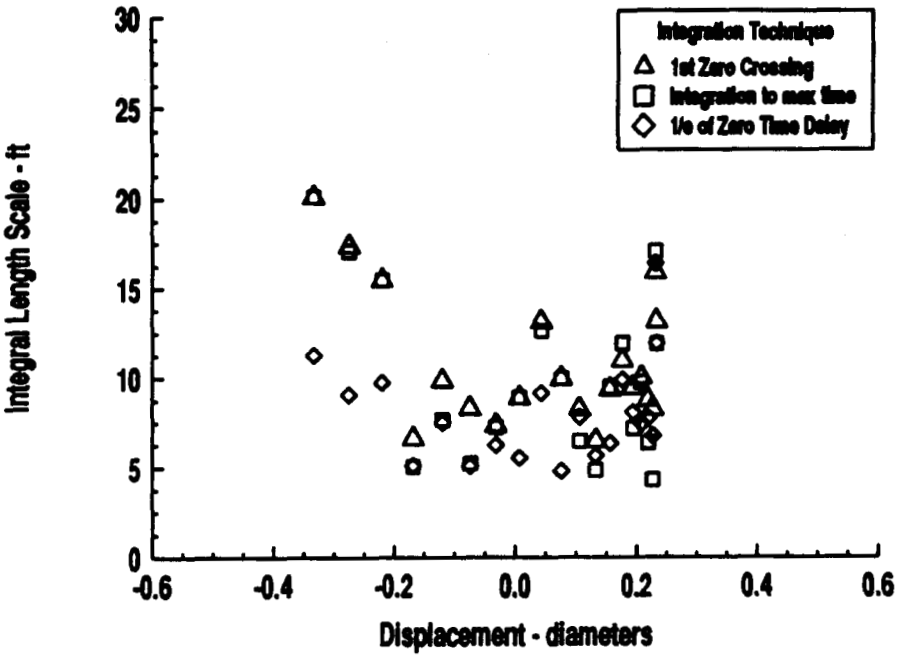

Figure 22: Axial Integral Length Scale as a Function of Position

Cross Correlation and Transverse Length Scales

The cross correlation function for the axial mean velocity displaced by a radial distance is described by:

$$R_{11}(0, r_z, 0, \tau) = \overline{u_1(0,0,0,t) u_1(0, r_z, 0, t+\tau)} \tag{7}$$

The normalized correlation coefficient is:

$$\tilde{R}_{11}(0, r_z, 0, \tau) = \frac{\overline{u_1(0,0,0,t) u_1(0, r_z, 0, t+\tau)}}{\overline{u_1 u_1}} \tag{8}$$

A typical cross correlation is shown in Figure 23. It is similar in form to the autocorrelation shown in Figure 19, but the coefficient does not approach unity for a zero time delay, unless the probe separation distance is very small. The coefficient is a maximum for a zero time delay, i.e. there is no phasing in the problem which increases the similarity of the two hot film signals.

A typical survey of cross correlation measured across the face of the rotor is shown in

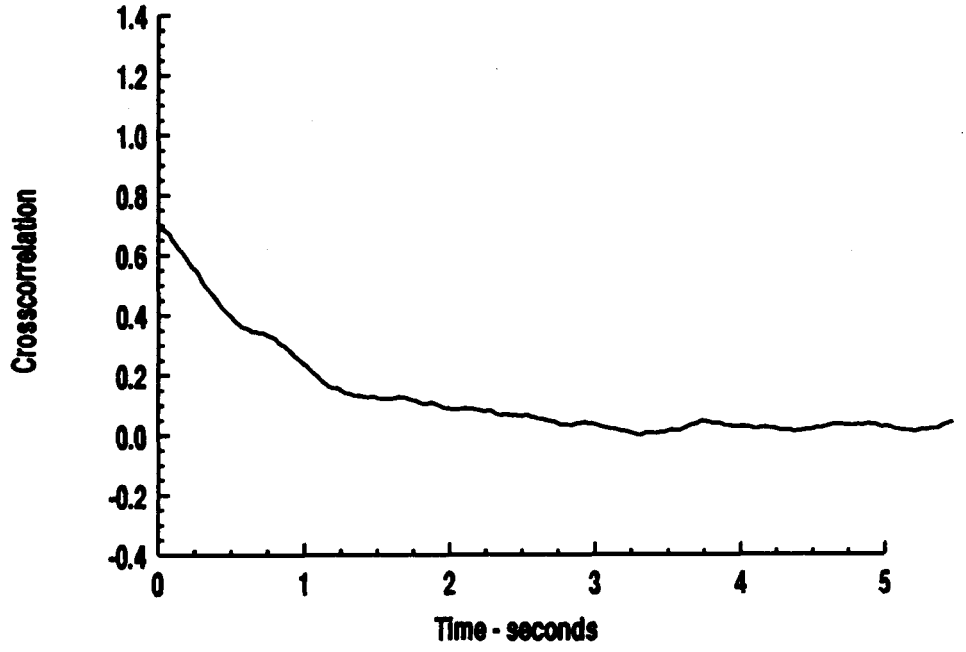

Figure 23: Typical Axial Turbulence Velocity Cross Correlation Coefficient

Figure 24. The correlation is seen to be highest when the probes are close together and decreases with both separation distance and delay time. The same data were presented in contour form in Figure 25. In this figure, contours of cross correlation coefficient are plotted in delay time and probe separation distance space. The maximum correlation is again seen to be for close separation distances and delay times.

The transverse length scale is determined from cross correlation measurements:

$$\ell_1^v = \int_0^\infty \tilde{R}_{11}(r_v) dr_v \tag{9}$$

where $\tilde{R}_{11}$ is evaluated at zero time delay.

A plot of the zero time delay cross correlation coefficient as a function of separation distance is shown in Figure 26. This same data can be seen in the zero time delay data in Figure 24. This data was integrated vs distance to obtain the transverse length scale.

Length scales in the axial direction were typically 30 times longer than the radial length scales, indicating that the turbulence into the rotor is highly non-isotropic.

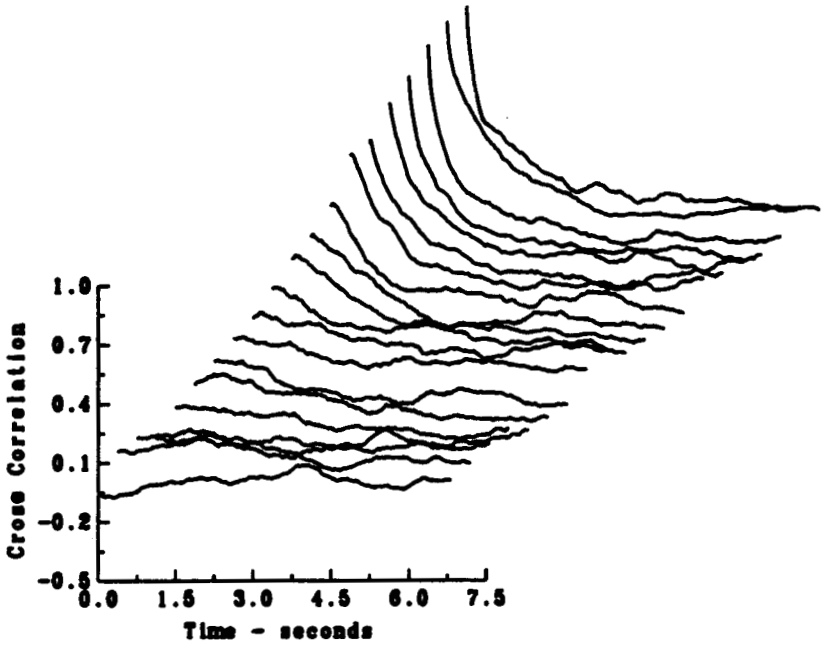

Figure 24: Axial Turbulence Velocity Cross Correlation Coefficient as a Function of Position

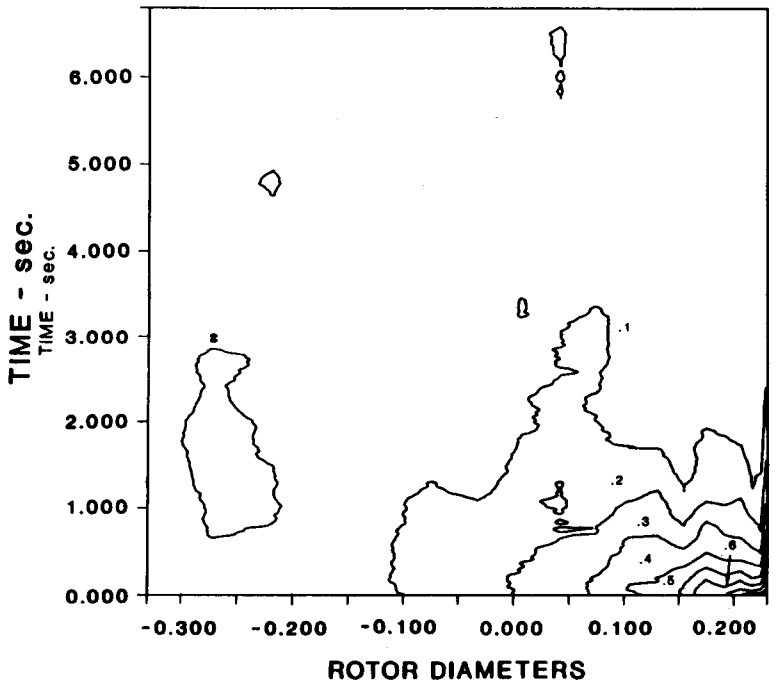

Figure 25: Contours of Cross Correlation Coefficient in Delay Time and Displacement Space

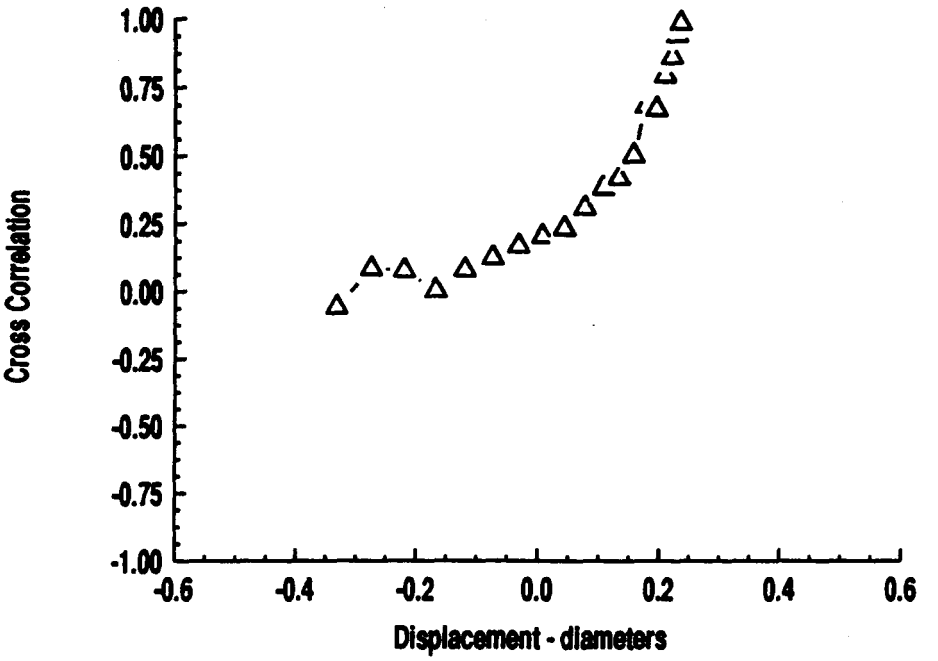

Figure 26: Zero Delay Time Cross Correlation Coefficient as a Function of Radial Position

Power Spectral Density

Figure 27 shows a plot of the power spectral density for a typical axial turbulent velocity signal. These data have been nondimensionalized by multiplying the spectral density by the mean velocity, dividing by the axial integral length scale and by the turbulence intensity. The frequency has been normalized by multiplying it by the axial integral length scale and dividing by the mean axial velocity. The normalizations were based on standard procedures used for turbulent flows. Also shown plotted on the graph is the von Karman spectrum, an isotropic spectrum. Since the measured turbulence is non-isotropic, the two spectra should not be identical and the degree of non-isotropy can be described by the difference in the two spectra.

Figure 28 show the power spectra for a typical 20 point survey taken in front of the rotor. The spectra all appear similar. The same data displayed in a contour plot in frequency and displacement space in Figure 29 also showed that the spectra are similar.

Cross Spectra

The cross spectrum is a similar quantity to the power spectrum. For an homogeneous,

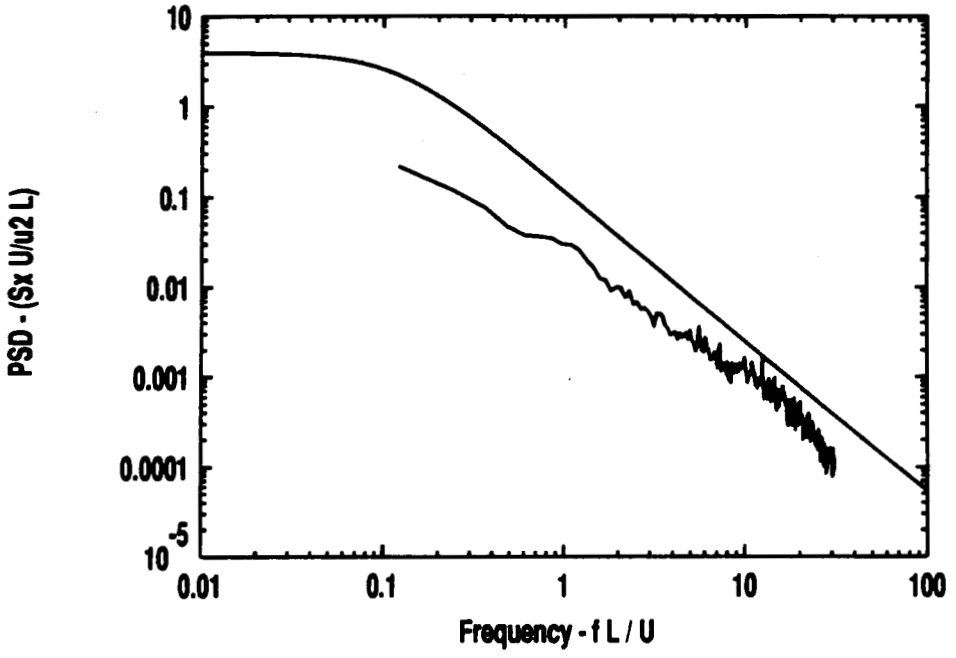

Figure 27: Typical Axial Turbulence Power Spectrum

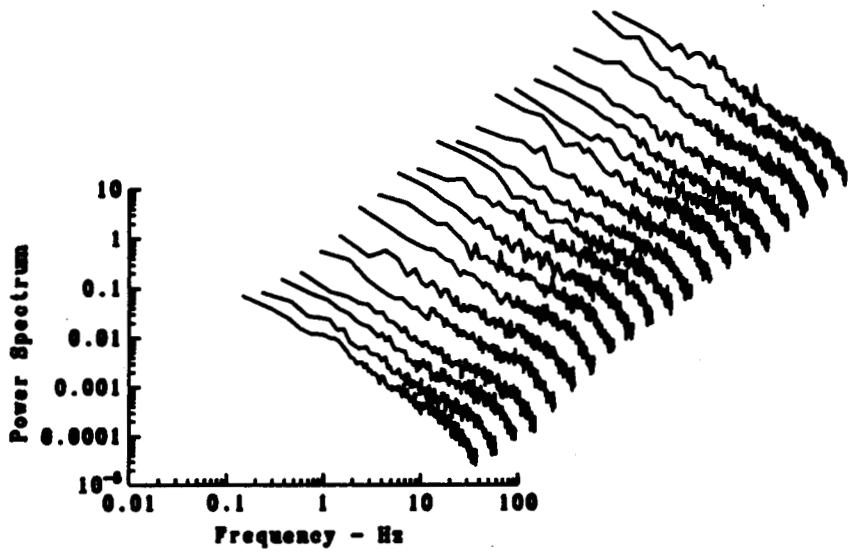

Figure 28: Axial Turbulence Power Spectrum as a Function of Radial Position

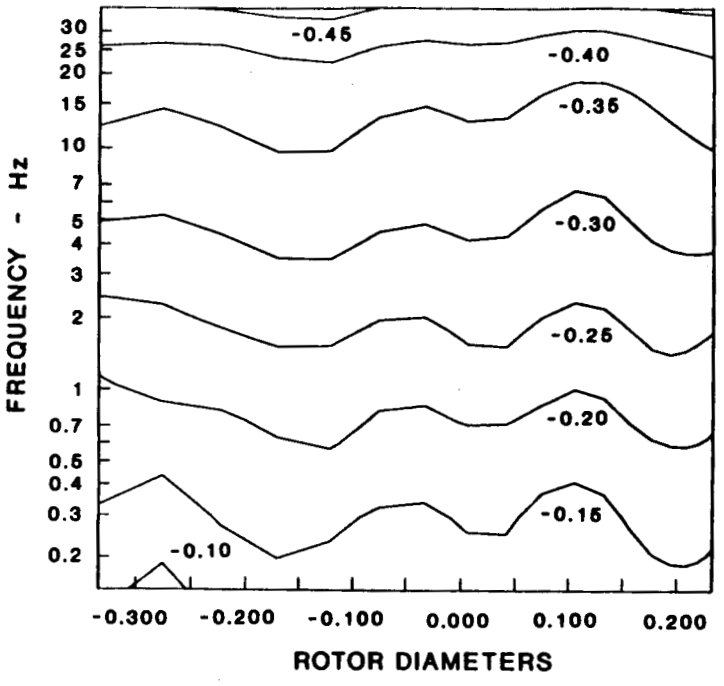

Figure 29: Contours of Power Spectrum as a Function of Frequency and Displacement

isotropic field, they are the same. A typical cross spectra plot for the axial component velocity of two probes separated in space in front of the rotor is shown in Figure 30. It is similar in shape compared to the power spectrum. Figure 31 shows the cross spectra for a typical 20 point survey in front of the rotor. There is considerably more scatter in the data at the far separation distances compared to close separation distances. A contour plot of the cross spectra on frequency and separation distance space is shown in Figure 32. The data presented in this figure have been smoothed using a tensioned spline in both cross spectra vs frequency and cross spectra vs separation distance. The cross spectra falls off with increasing frequency and separation distance.

TURBULENCE INGESTION NOISE MEASUREMENTS

Basic Characteristics

As summarized in Table 1, acoustic data were acquired over a range of blade pitch angles and tip Mach numbers. A typical turbulence ingestion spectrum is shown in Figure 33. The

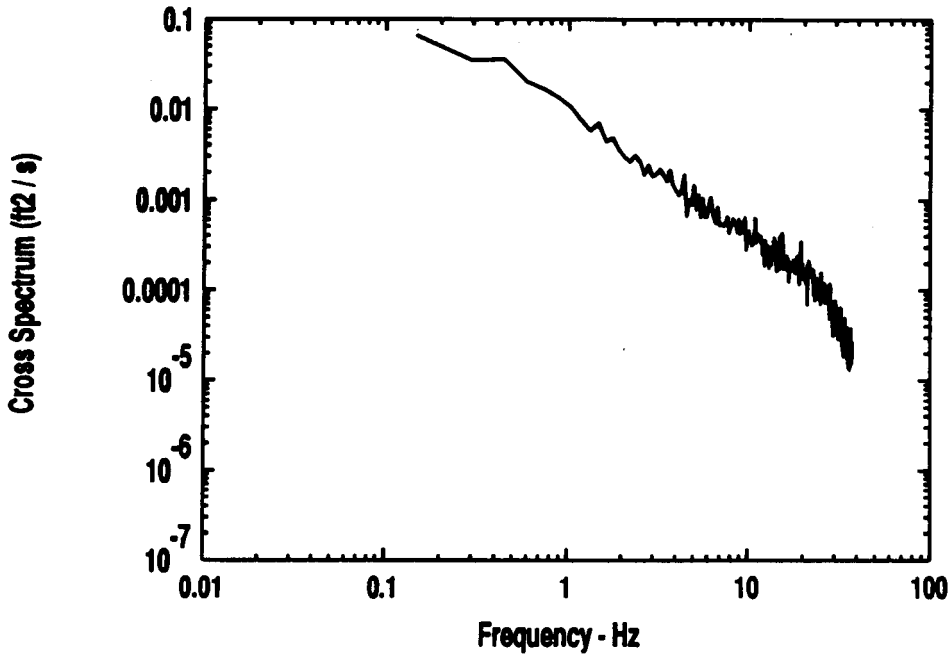

Figure 30: Typical Axial Turbulence Cross Spectrum

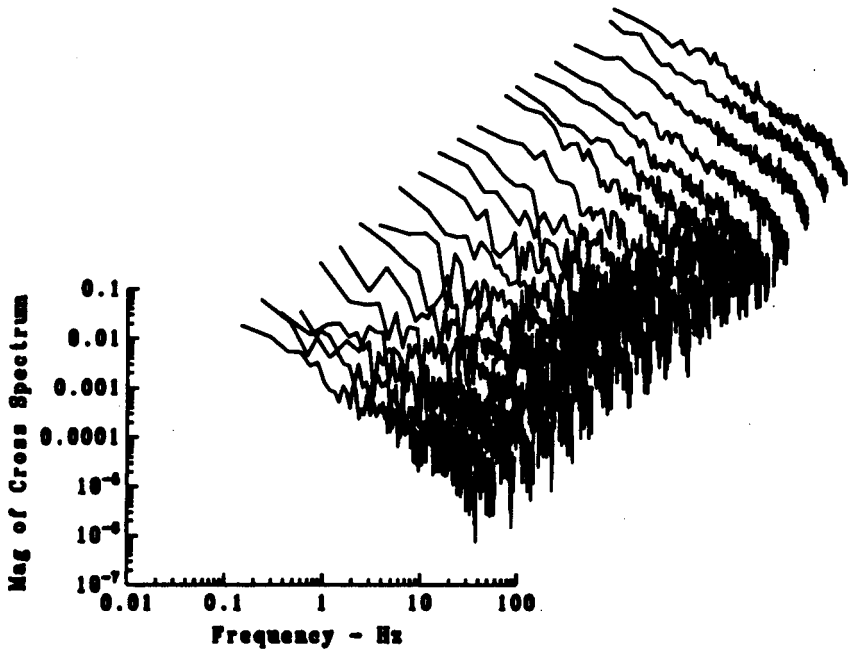

Figure 31: Axial Turbulence Cross Spectrum as a Function of Radial Position

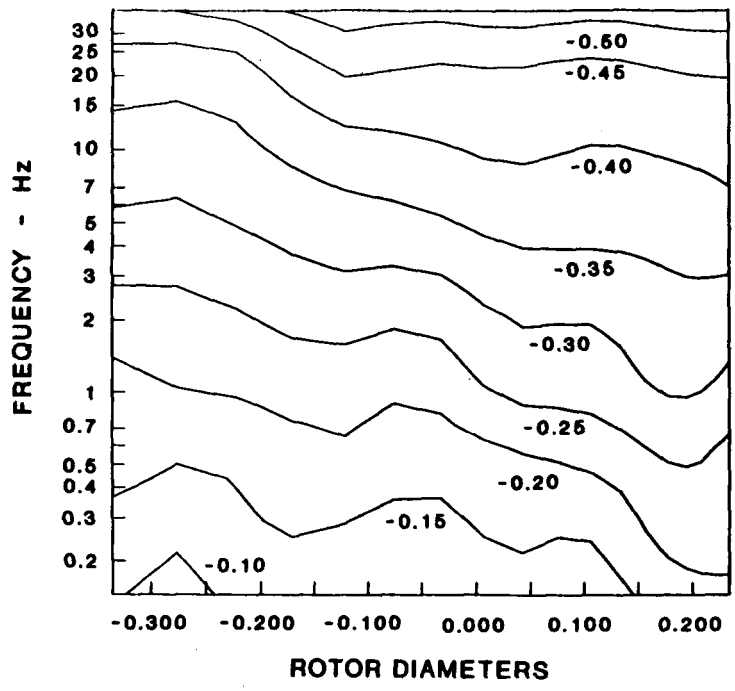

Figure 32: Contours of Cross Spectrum as a Function of Frequency and Displacement

spectra shows harmonics of blade passage frequency evident out to at least 20 harmonics before changing to a broadband character.

Figure 34 shows ten spectra obtained from the polar microphone arc for one operating condition. The signatures appear similar in characteristic except for two features. Near the plane of rotation where turbulence ingestion noise is expected to approach zero, the level of the blade passage frequency increases above the other harmonics. This increase is thought not to be caused by turbulence ingestion noise, but is the result of other noise mechanisms, such as unsteady thickness noise. Another feature of the signatures appears near the rotor axis. Here, a slight waviness of the spectrum is apparent in the broadband portion of the spectrum.

Polar Directivity

The polar directivity of the far field turbulence ingestion noise is shown in Figure 35. Here, the blade passage frequency (BPF), the 5th harmonic, the 10th harmonic and the 14th harmonic are shown for a 5° pitch angle and a tip speed of 144 m/s. Except for the BPF, a common trend is apparent with polar directivity. The directivity reaches a maximum slightly off the axis of rotation, and drops off towards the plane of rotation.

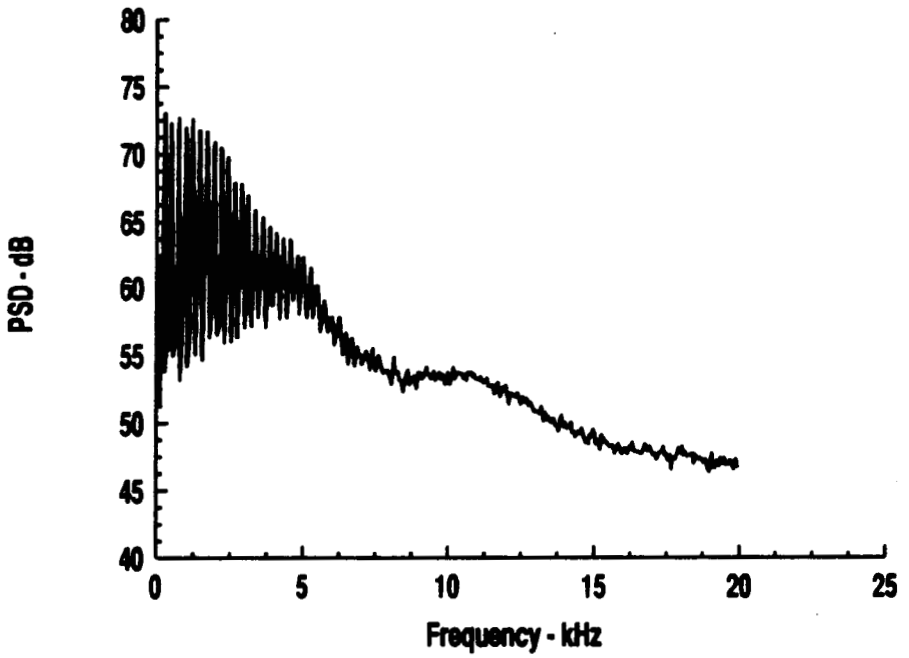

Figure 33: Turbulence Ingestion Noise Spectra - V_{tip} = 144 m/s, 5° *pitch*, 0 ° polar directivity angle

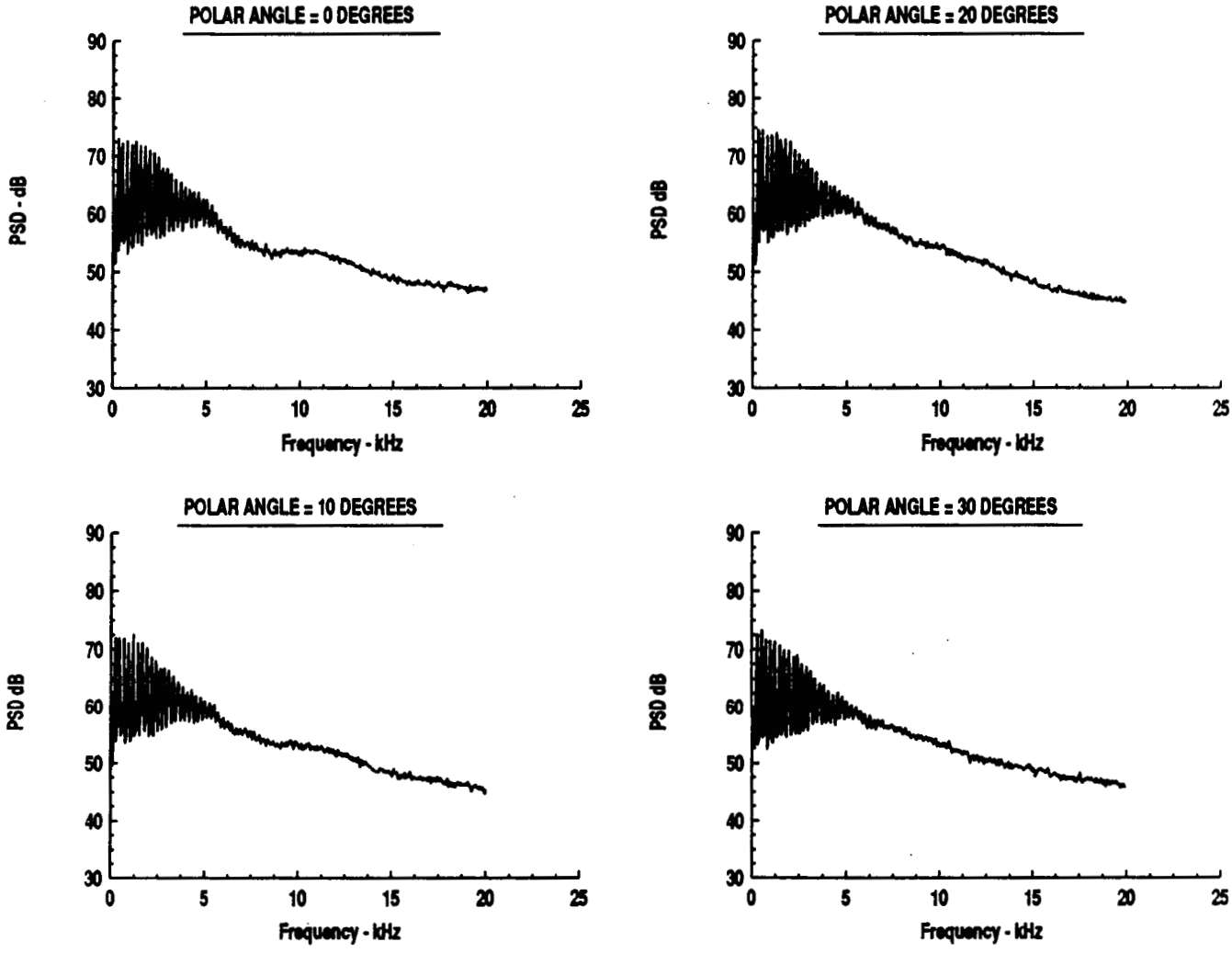

Figure 34: Polar Directivity Characteristics of Noise Spectra - V_{tip} = 144 m/s, 5° pitch

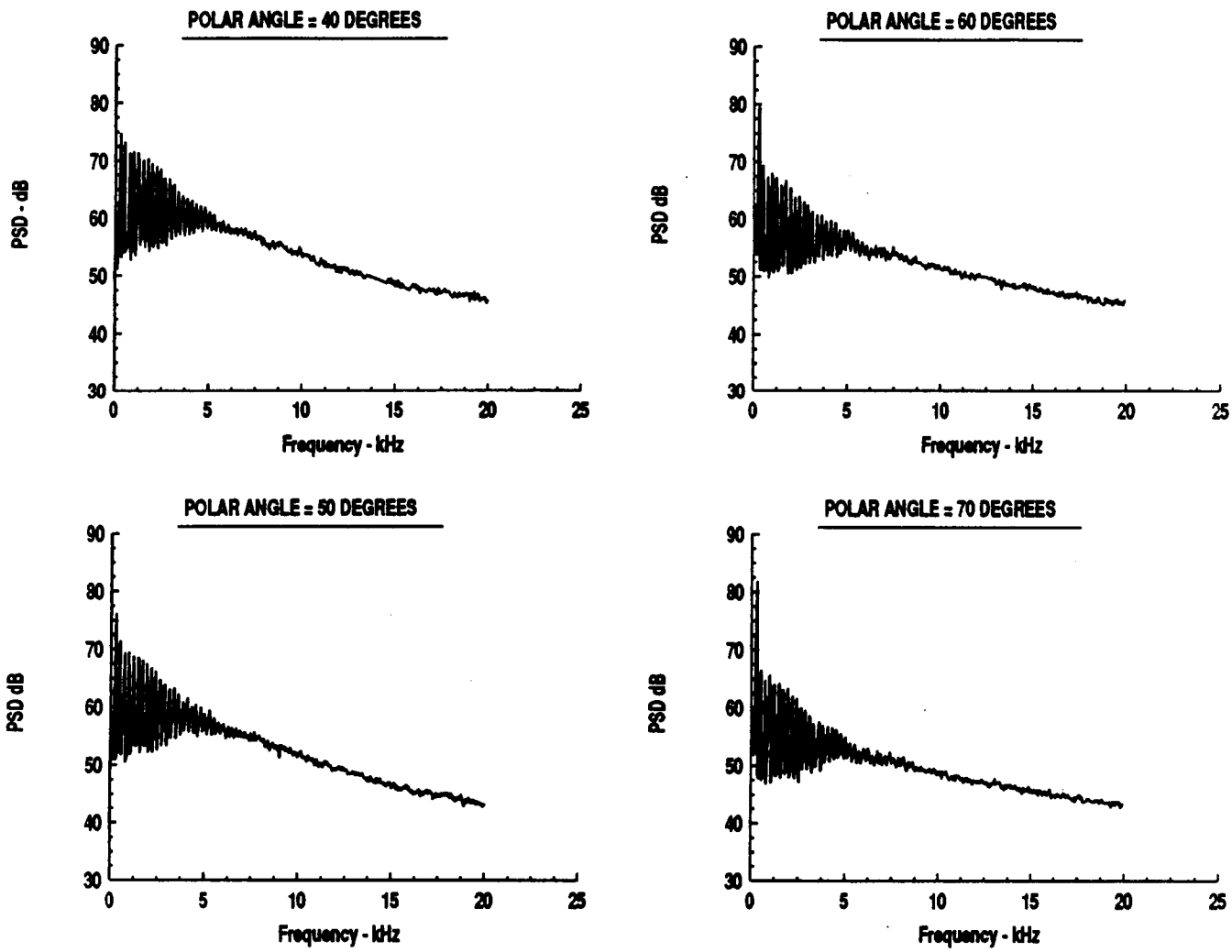

Figure 34: Continued

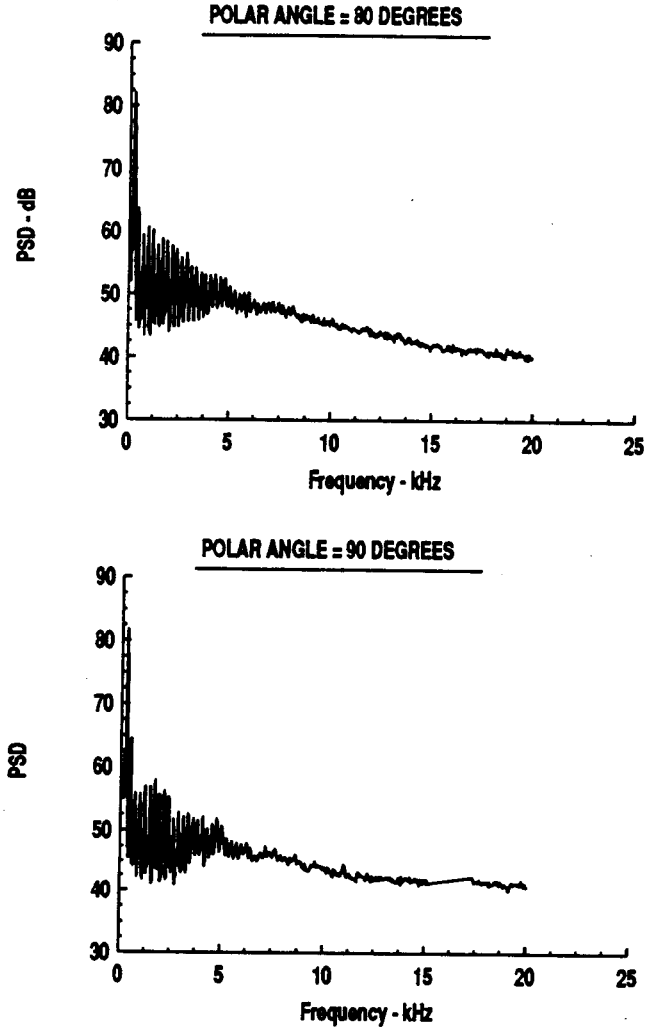

Figure 34: Concluded

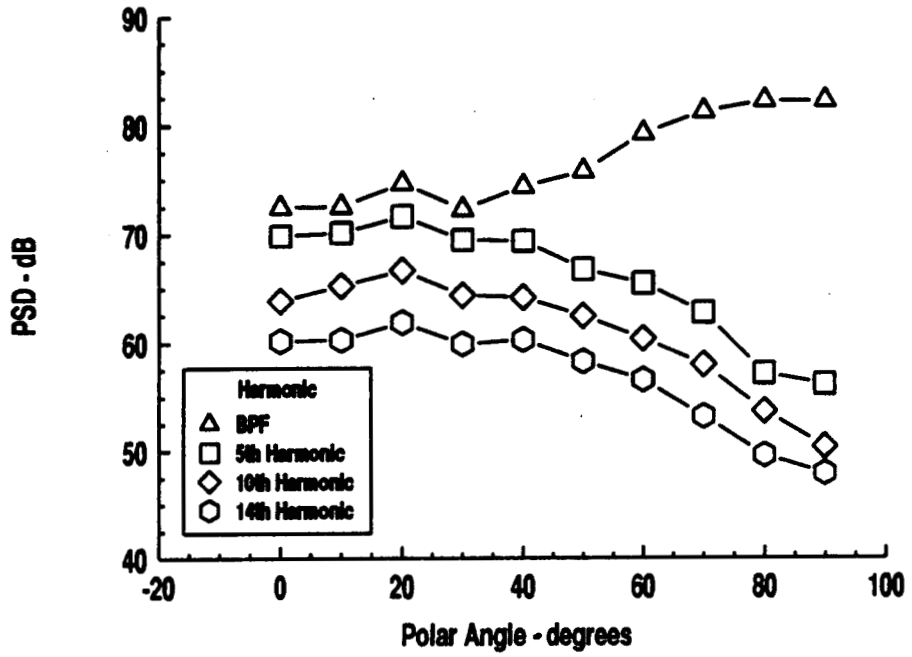

Figure 35: Polar Directivity for Several Harmonics - V_{tip} = 144 m/s, 5° pitch

Blade Pitch Angle

Increasing blade pitch angle increases the sound pressure level, as shown in Figure 36. This plot shows the effect of pitch angle change on the 10th harmonic for four different blade tip speeds. The 10th harmonic was chosen as a representative harmonic.

Tip Speed

Figure 37 shows the effect of changing tip speed on the 10th harmonic of blade passage frequency for the three blade pitch angle settings used in the test. Increasing tip speed increases the measured sound pressure level.

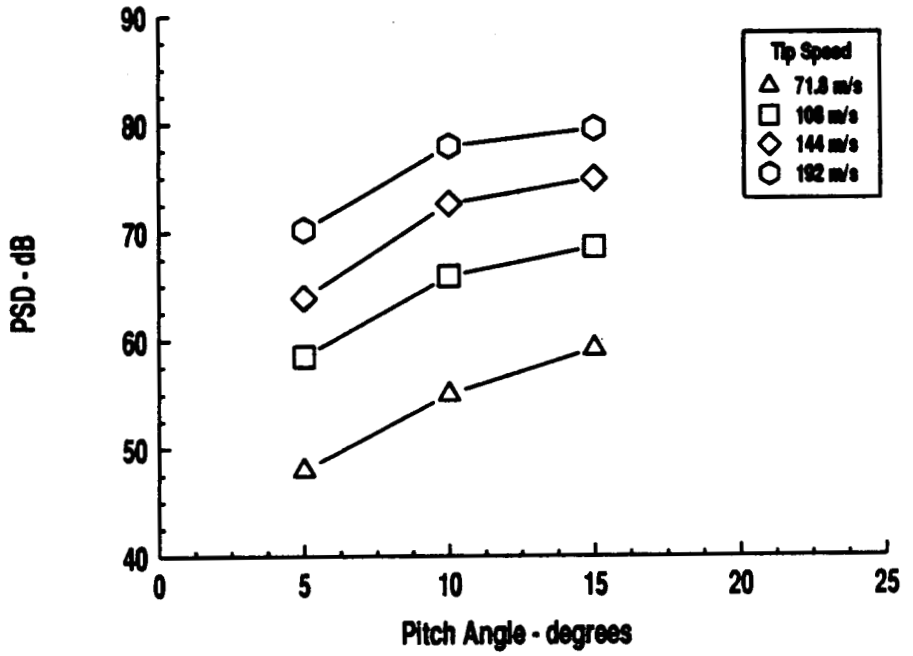

Figure 36: Effect of Pitch Angle on 10th Harmonic Levels

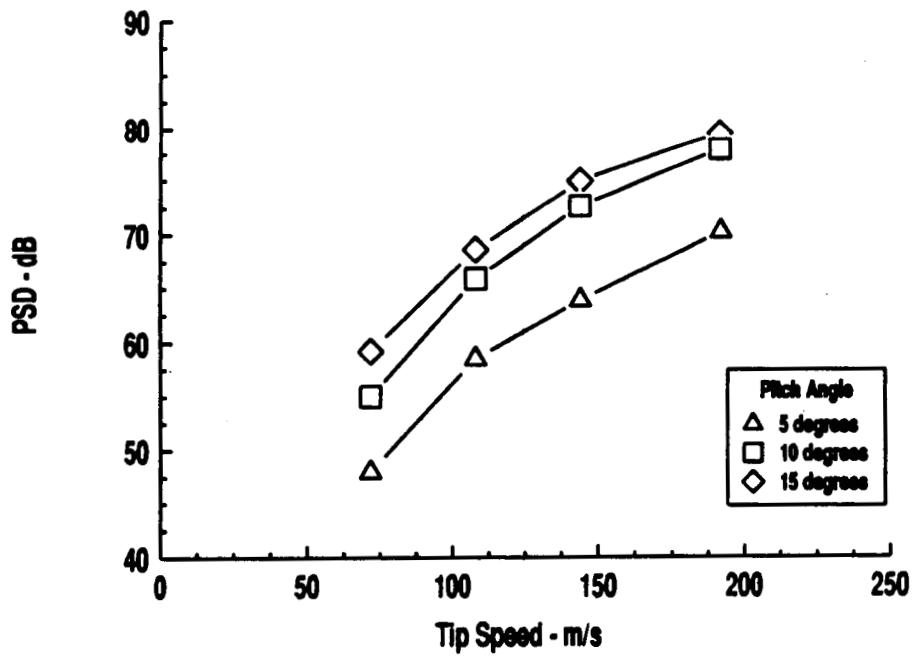

Figure 37: Effect of Blade Tip Speed on 10th Harmonic Levels - V_{tip} = 144 m/s, 5° pitch

TURBULENCE INGESTION NOISE PREDICTION PROGRAM

Approach

The purpose of this study was to experimentally assess a non-isotropic, non-homogeneous turbulence ingestion noise theory of Amiet. This theory has been used as part of a larger effort to develop a prediction methodology for helicopter rotor noise due to the ingestion of atmospheric turbulence. The focus of this work is a computer code, developed according to ANOPP standards, which has been transferred to NASA for incorporation into ROTONET. With the prediction methodology completed (References [8] – [11]) the present experimental measurement was conducted to determine the applicability of the analysis.

The theory for the atmospheric turbulence prediction and mean flow and turbulence contraction is described in Reference [8]. The noise calculation theory is described in Reference [9]. Reference [10] is a users manual for the atmospheric turbulence and the mean flow and turbulence contraction programs. A users manual for the noise calculation program is described in Reference [11].

The prediction method incorporates an atmospheric turbulence model, a rotor mean flow contraction model and a rapid distortion turbulence model which together determine the statistics of the non-isotropic turbulence at the rotor plane. Critical to the turbulence contraction model is the inclusion of a rotor mean flow model which predicts the turbulence vorticity distortion during the rotor in-flow process.

A generalized acoustic source model was used to predict the far field noise generated by the non-isotropic flow incident on the rotor. Absolute levels for acoustic spectra and directivity patterns are calculated without the use of empirical or adjustable constants. This procedure was extended from a previous prediction procedure [4] to include non-homogeneous turbulent inflow to the rotor.

Assumptions

The purpose of the present study was to devise an experiment which would allow comparison of measured non-isotropic, non-homogeneous turbulence ingestion noise against Amiet's theory. The analysis for atmospheric turbulence ingestion was written such that turbulence properties of the atmosphere are specified at infinity and the properties at the rotor face are calculated using a rapid distortion approach. In the current experiment,

properties were measured directly at the rotor face. A method had to be devised to rearrange the measured data into a form acceptable to the acoustic prediction program.

While the noise prediction theory is capable of dealing with nonhomogeneous, non-isotropic turbulence, it would require measurements over a large number of points on the rotor. While in concept it is possible to do this, it is not practical. Therefore, it was decided to compare only the homogeneous theory against the experiment.

Two approaches are possible depending on the amount of approximation acceptable and the type and quantity of data available. The more exact approach involves specifying the cross spectra at numerous locations above the rotor face. Measurements would be required over a large number of different locations since the flow into the rotor is nonhomogeneous, even for the current, simple, recirculating, hover operating condition.

Since in the current experiment, the cross spectra were obtained over a limited number of points, the cross spectra data must be surface fit as a function of location, since the program requests the amplitude of the cross spectra at any frequency and location. Also, the program may request the cross spectra at a frequency that is higher than the measured data, in which case an extrapolation procedure would be required. The turbulence ingestion noise computer program presented in reference [4] would also have to be modified in order to accept the measured cross spectrum.

This approach was pursued initially until the above implications of using it became clear. In leu of the difficulties associated with this approach and the limited amount of time available for data reduction, an alternative approach was executed.

The alternative approach used the turbulence ingestion noise prediction program in its "production" version, the one supplied to Langley as part of this contract effort which will be incorporated into the ROTONET noise prediction program.

The following assumptions are made for this calculation procedure:

- isotropic turbulence upstream
- upstream von Karman spectra
- rotor flow is homogeneous
- rotor flow is non-isotropic
- noise is produced near the blade tip

Formulation of Inputs

This program assumes that the turbulence far upstream of the rotor is isotropic and

is deformed into non-isotropic turbulence as it is convected into the rotor. The upstream turbulence spectrum is described by the von Karman model. The transformation of the turbulence from isotropic to non-isotropic turbulence is described by a deformation tensor. In the ANOPP version, this deformation tensor is calculated by a streamline tracing technique. Since the streamline coordinates were not known in the current experiment, a simplified, but still non-isotropic, turbulence description model was utilized. For a pure contraction with no skewing or turning of the streamlines, a non-isotropic, diagonal, distortion tensor can be described by:

$$\left[\frac{\partial x_i}{\partial \xi_j}\right] = \begin{bmatrix} 1/\ell_1 & 0 & 0 \\ 0 & 1/\ell_2 & 0 \\ 0 & 0 & 1/\ell_2 \end{bmatrix} \tag{10}$$

where ℓ_1 is the longitudinal or streamwise integral length scale and ℓ_2 is the lateral or cross stream integral length scale. The longitudinal length scale describes the length of a typical eddy in the streamwise direction whereas the lateral length scale describes the width of a typical eddy entering the rotor. This type of deformation was considered by Ribner and Tucker[12].

In addition to the length scales, the axial and radial mean velocities, and the axial turbulence intensity at the rotor are also required inputs to the noise prediction theory. Since a homogeneous assumption was made, only a single value of each parameter can be input. Either a single representative value can be chosen, or values averaged over the rotor face can be used. Since higher noise levels are produced in high speed regions near the blade tip and less noise is produced near the hub where both inflow velocities and blade speeds are lower, it was decided to use representative measurements from near the blade tip for input into the noise prediction program.

Parameter Sensitivity

There are five aerodynamic measurements which influence the predicted noise:

- axial mean velocity
- radial mean velocity
- axial integral length scale
- radial integral length scale
- streamwise turbulence intensity

A study was undertaken to determine the sensitivity of each parameter. An average value was chosen as inputs for the five experimental parameters and then each parameter

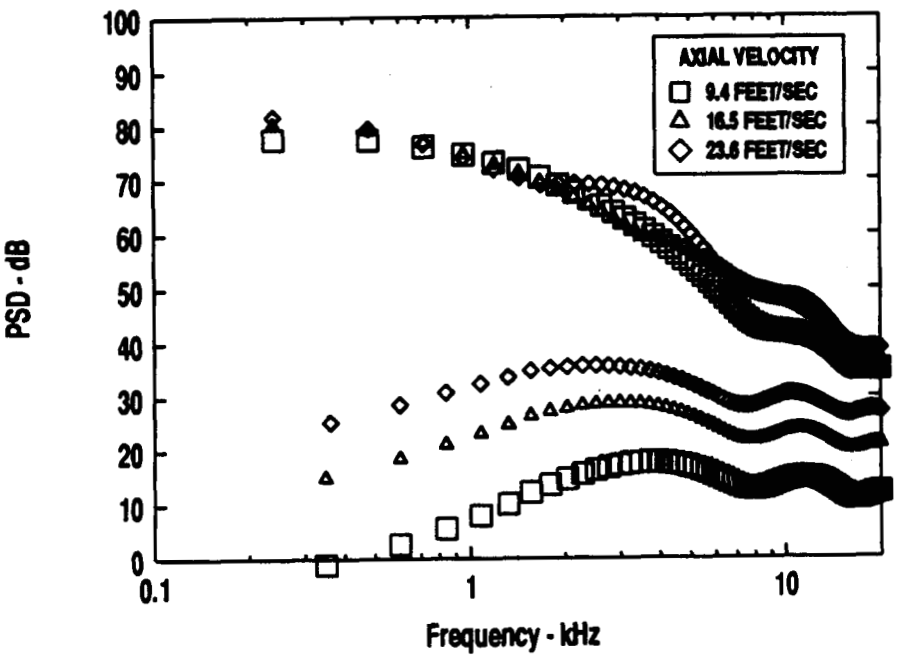

Figure 38: Sensitivity of Mean Axial Velocity on Predicted Sound Pressure Levels

was varied from a minimum value from any position on the rotor from the experimental data to a maximum value, holding the other parameters at their average value.

Figure 38 shows the sensitivity of the predicted sound pressure level spectra to the mean axial velocity. In order to avoid confusion by overplotting, only the peaks and troughs of the harmonics are shown for the three cases. Varying the axial velocity has a large effect on the troughs of the harmonics. There is little sensitivity for axial velocity variation for the peaks of the harmonics, especially at the lower frequencies. The sensitivity of the predicted noise output to variations in radial velocity is insignificant over the range of values tested, as shown in Figure 39.

The sensitivity of the predicted sound pressure level spectra for axial and radial integral length scales is shown in Figures 40 and 41. Very little effect is noted for either length scale for frequencies below 3 kHz. Little effect is noted for the troughs for the radial length scales, and only a small effect is noticed for the troughs on the axial length scale. There is a rather large effect on the spectrum peaks for frequencies above 3 kHz for both the axial and radial length scales.

The most sensitive parameter over the entire frequency range is the turbulence intensity shown in Figure 42. A 12 dB variation in sound pressure level is noted for a change in turbulence intensity from 2.25% to 10%.

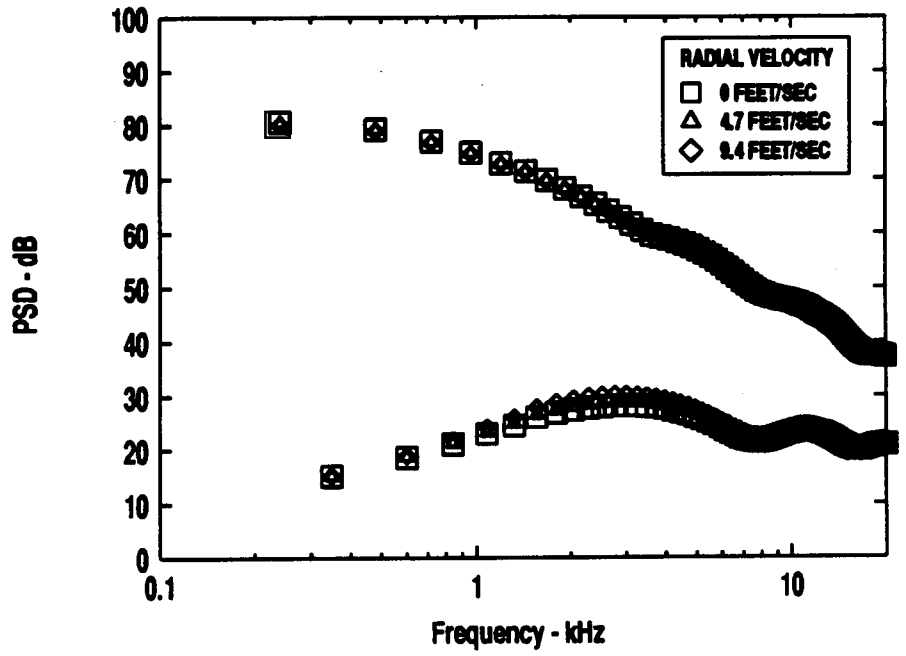

Figure 39: Sensitivity of Mean Radial Velocity on Predicted Sound Pressure Levels

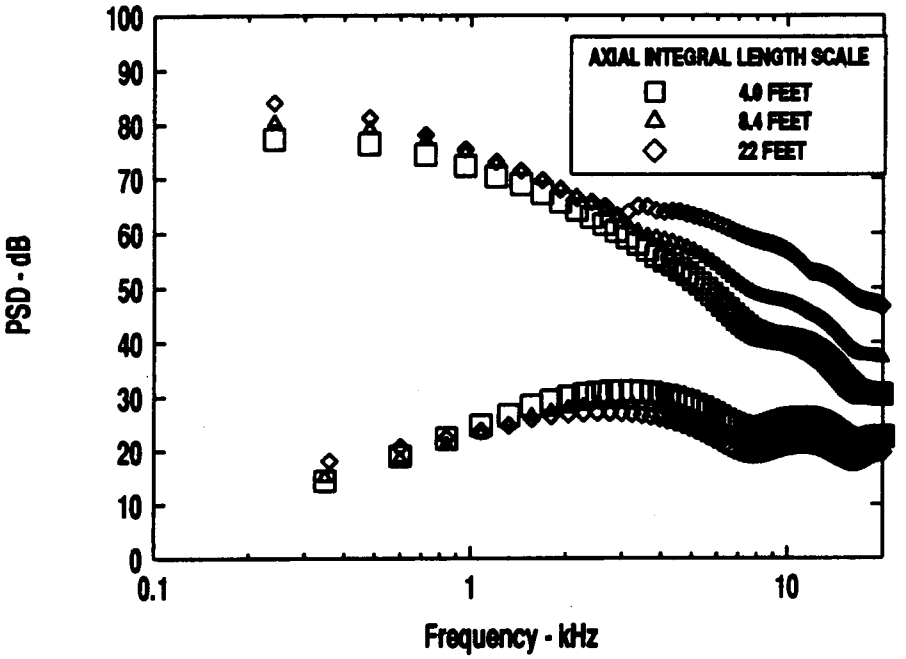

Figure 40: Sensitivity of Axial Integral Length Scale on Predicted Sound Pressure Levels

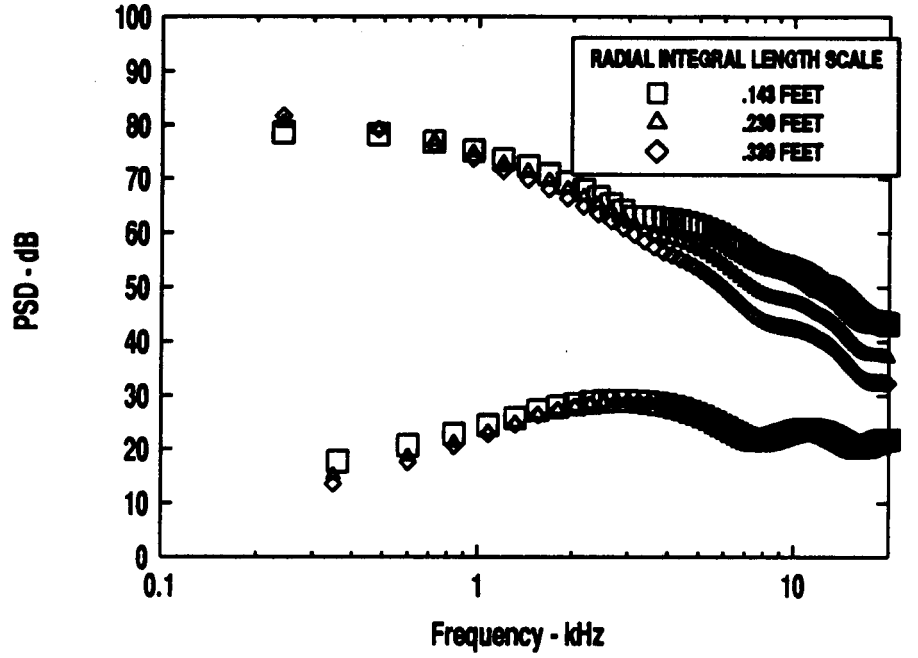

Figure 41: Sensitivity of Radial Integral Length Scale on Predicted Sound Pressure Levels

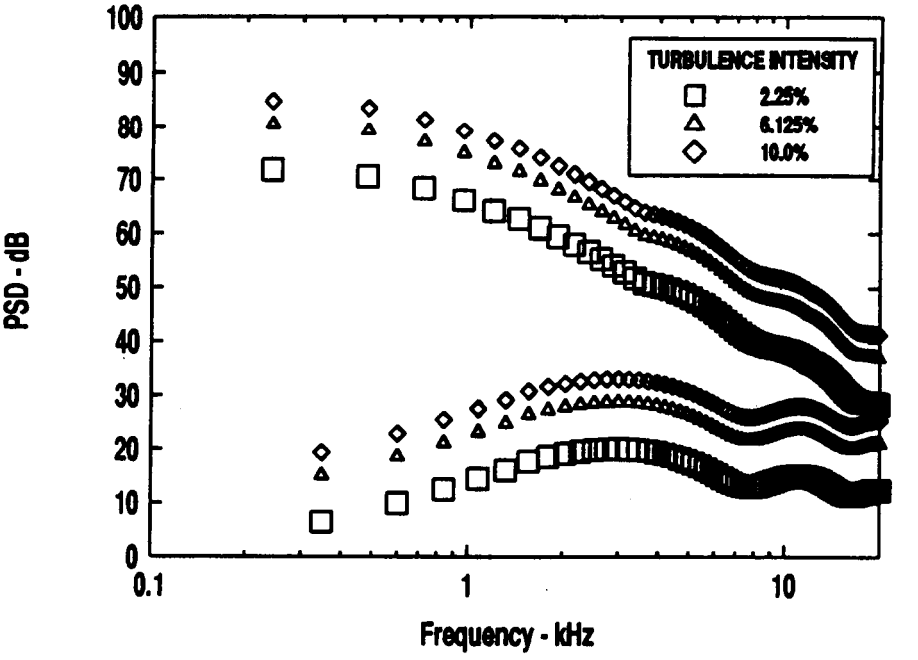

Figure 42: Sensitivity of Input Turbulence Intensity on Predicted Sound Pressure Level

Theory-Experiment Comparison

Predictions were made using Amiet's theory, using input values taken from measurements near the rotor blade tip, where most turbulence ingestion noise is assumed to be produced. The comparison between the measured and predicted peak spectra is shown in Figure 43. Ten directivity angles are shown. In general, the theory overpredicts the lower harmonics and under predicts the higher harmonics, although the agreement is quite good. The theory predicts much lower peaks and carries harmonics to much higher frequency than the experiment showed. The only directivity angle where the agreement is not good is at 90°, in the plane of the rotor. The reason for this is that other noise mechanisms are more important than turbulence ingestion noise for this directivity.

The predicted sound pressure level as a function of polar angle for the blade passage frequency, the 5th harmonics, the 10th harmonic and the 14th harmonic is shown in Figures 44, 45, 46 and 47 respectively.

Except for the blade passage frequency plot, the theory is in excellent agreement with the measurements in both trends and level. The most discrepancy occurs in the rotor plane where other noise mechanisms such as unsteady thickness noise may dominate. The best agreement between theory and experiment occurs for the 5th harmonic. The theory does not predict the trend of the experimental data for the blade passage frequency although the absolute levels are not far wrong.

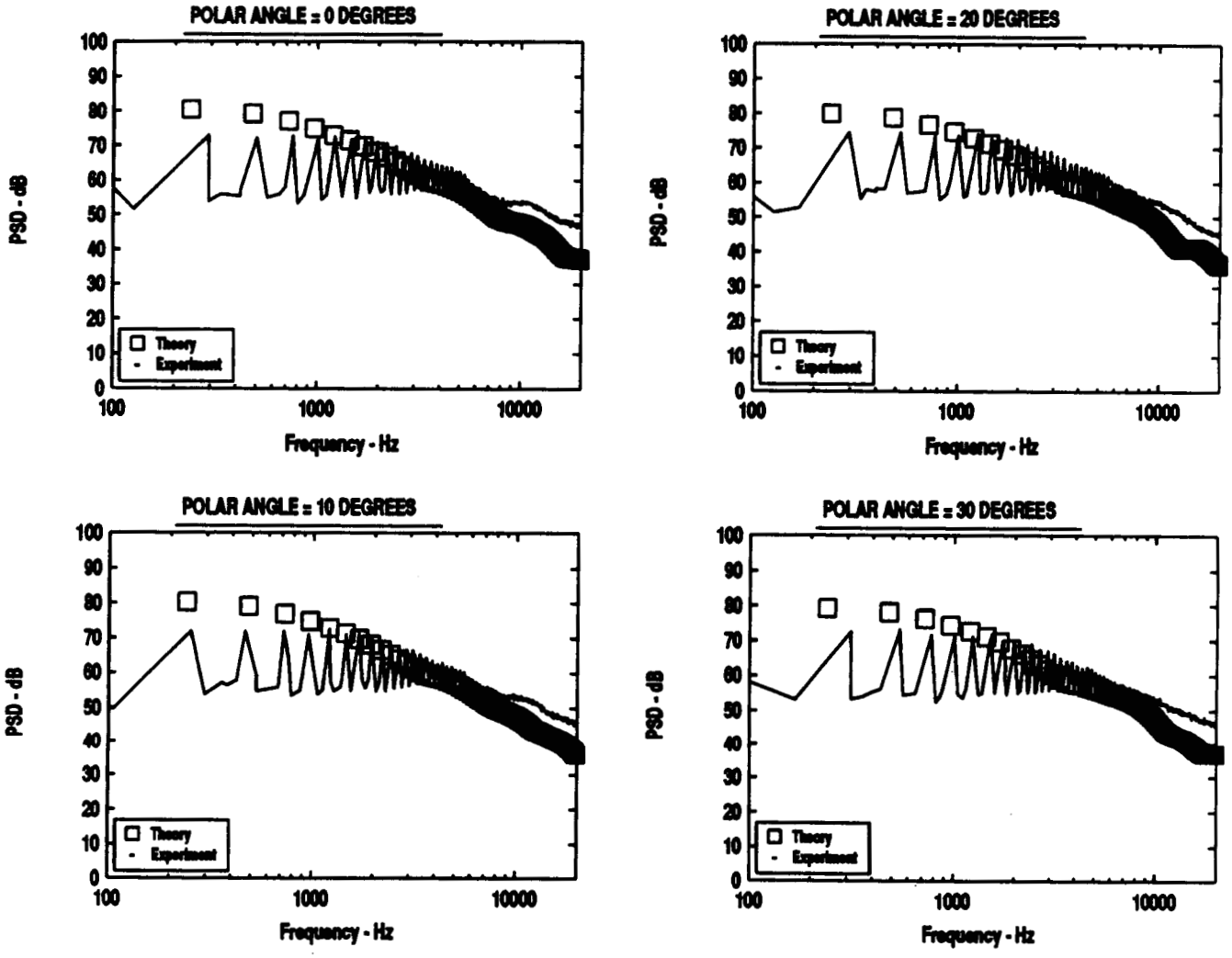

Figure 43: Predicted Peak Levels vs Measured Spectra

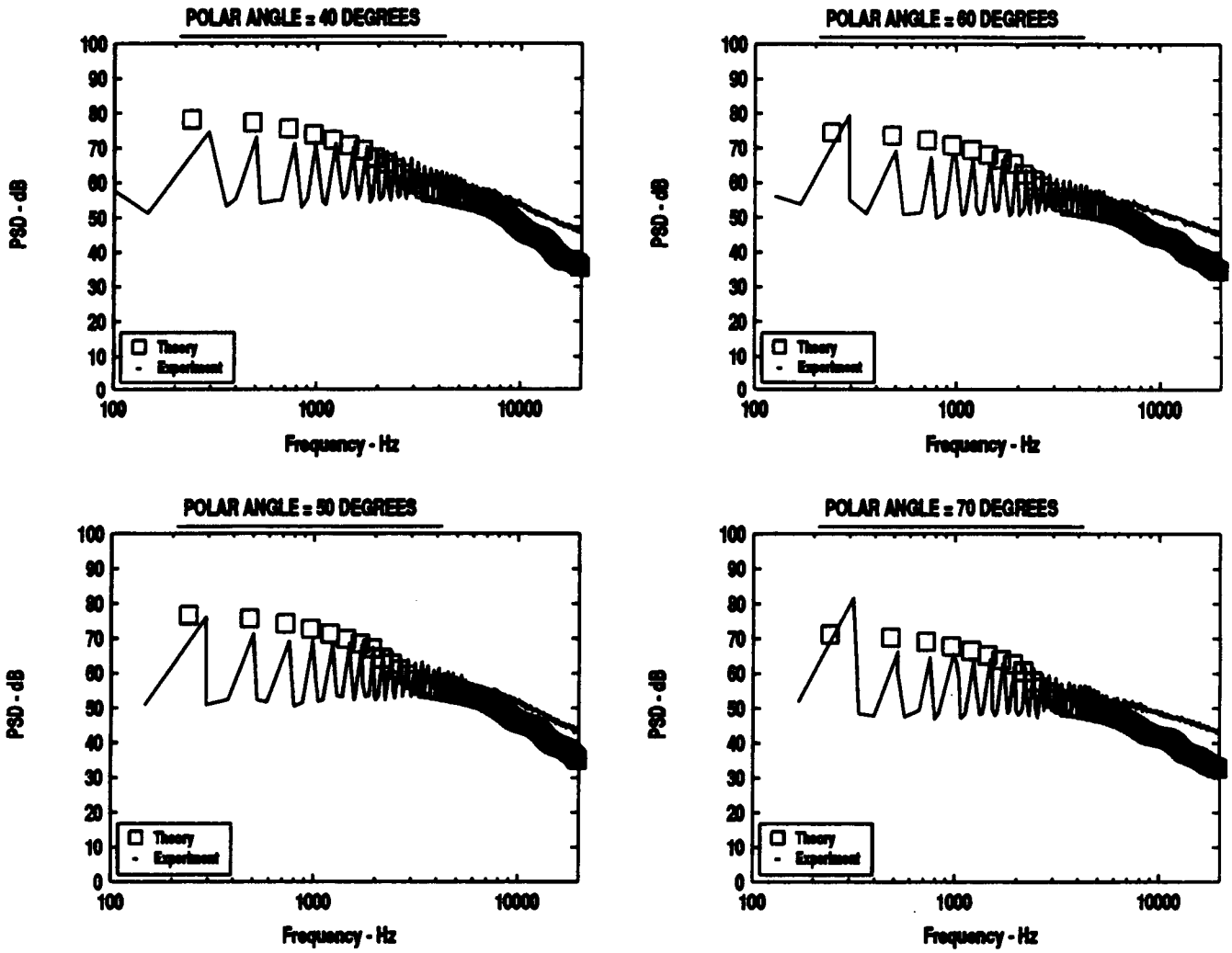

Figure 43: Continued

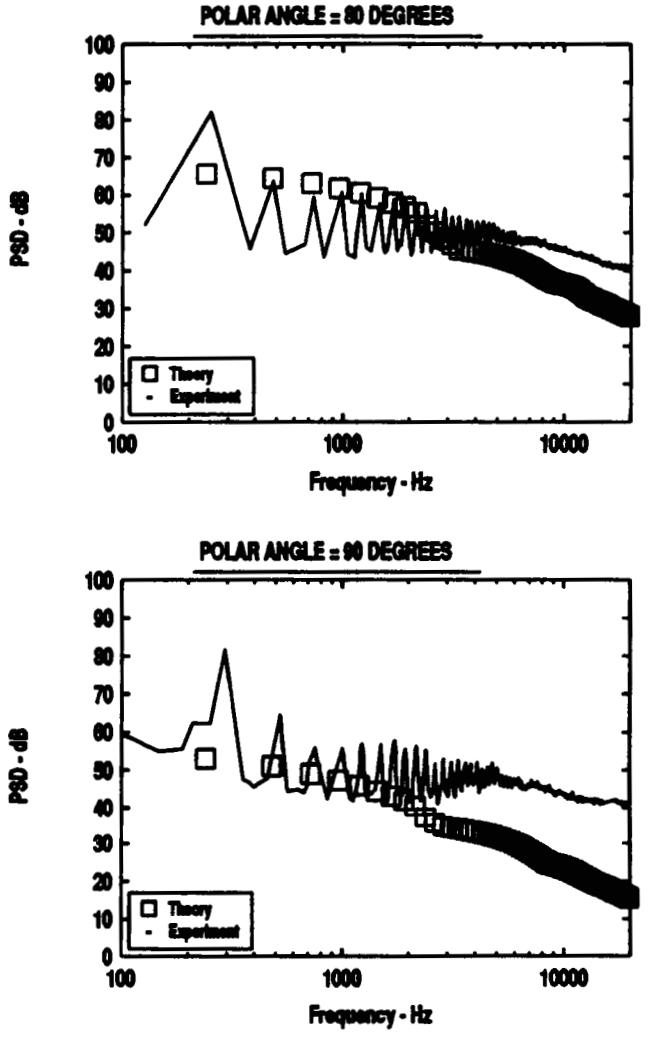

Figure 43: Concluded

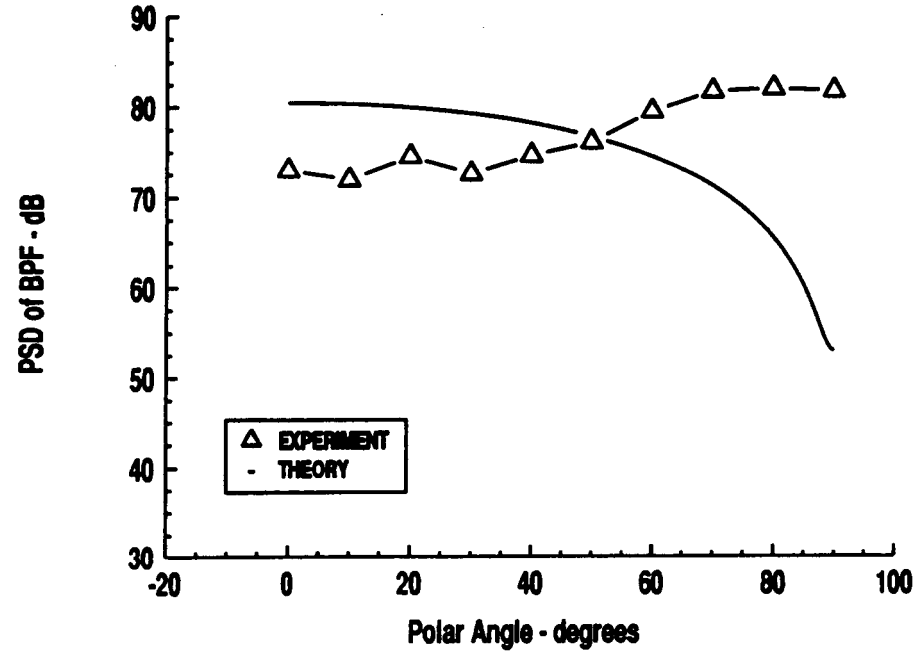

Figure 44: Predicted vs Measured Blade Passage Frequency Levels

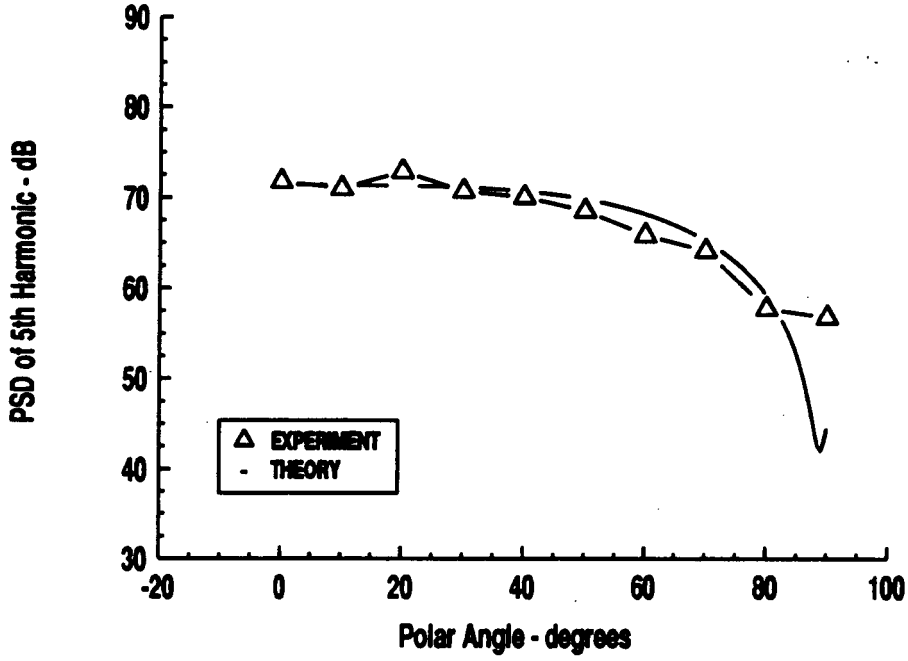

Figure 45: Predicted vs Measured 5th Harmonic Levels

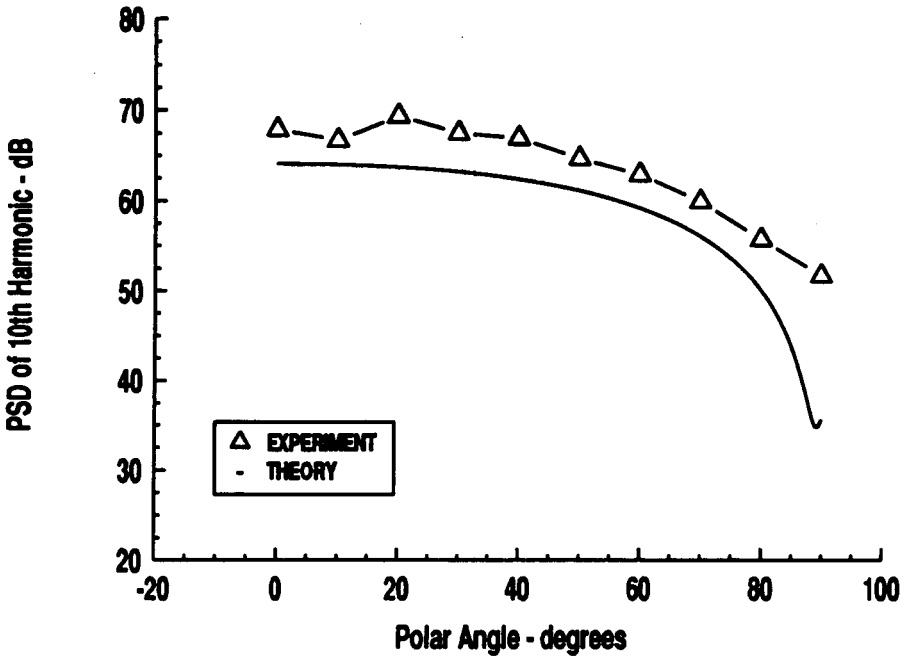

Figure 46: Predicted vs Measured 10th Harmonic Levels

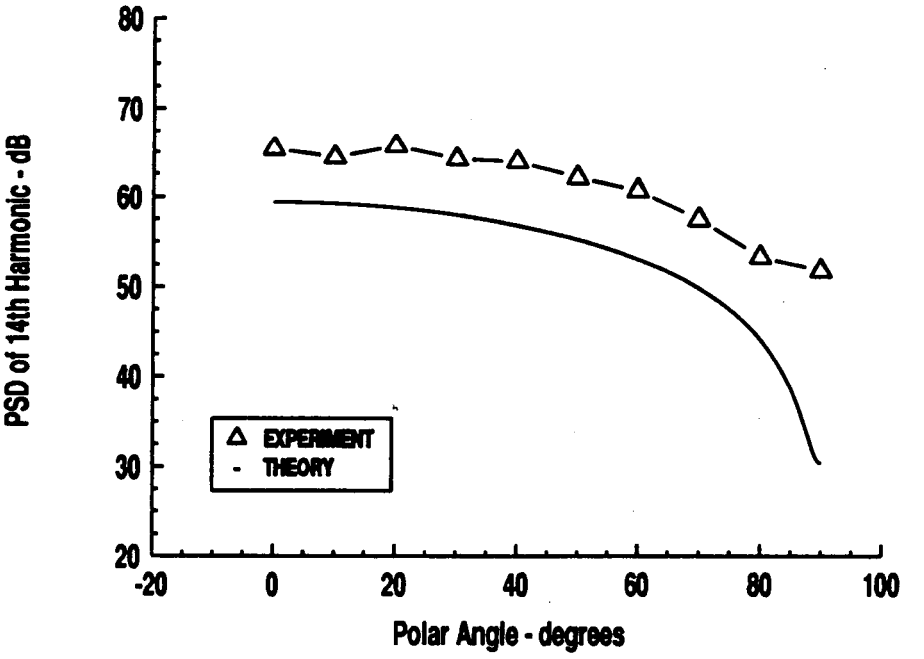

Figure 47: Predicted vs Measured 14th Harmonic Levels

CONCLUSIONS

A model helicopter rotor was tested in an anechoic chamber in hover in a closed chamber so that non-isotropic turbulence generated by the rotor was reingested by the recirculating flow into the rotor. An analytical procedure was developed to use measured non-isotropic aerodynamic properties at the rotor to predict the noise due to turbulence ingestion. The noise generation model is based on a simplification of an analysis and computer code previously developed by Amiet for non-isotropic turbulence. The following conclusions were drawn from this study:

- *The turbulence at the rotor was non-isotropic. Integral length scales computed from measured auto and cross correlations determined that typical eddies were 30 times longer than they were wide. Measured power spectra were similar to isotropic von Karman spectra but offset, indicating a degree of non-isotropy.*

- *Turbulence ingestion noise was the dominant noise mechanism in hover. Although this test was carried out on a model rotor, the results should apply equally well to a full scale helicopter in hover providing there is no interaction between the main and the tail rotors.*

- *The measured noise spectrum showed quasi-tonal noise out to at least 20 harmonics, before changing to broadband in character. The polar directivity of the measured noise spectrum peaks at about 20° off the rotor axis and falls to a minimum in the plane of the rotor for the 5th through the 14th harmonics. The noise level at the blade passage frequency increases as the polar angle approaches the rotor plane.*

- *Increasing blade pitch angle increases the measured sound pressure level for all measured tip speeds. Increasing blade tip speed increases the measured sound pressure level for all measured blade pitch angles.*

- *The simplified non-isotropic prediction procedure which has been developed can be used to reasonably predict absolute sound pressure levels for turbulence ingestion noise in hover, given 5 input parameters: axial velocity, radial velocity, axial integral length scale, radial integral length scale, and turbulence intensity.*

- *The predictive procedure was found to be sensitive to three inputs: turbulence intensity, and the two length scales. The sensitivity of the length scales was confined mainly to high frequencies, while changes to the turbulence intensity affected the entire spectrum. A change in turbulence intensity from 2.25% to 10% increased the predicted sound pressure level by 12 dB.*

- *The general agreement between the non-isotropic noise prediction theory and the experiment was good, although the theory generally overpredicts the quasi-tonal low to mid*

range frequencies and underpredicts the higher broadband signals. The measured polar directivity trends were matched by the prediction for low to mid harmonics, except in the plane of the rotor. At this angle, other noise generation mechanisms are more important, such as unsteady thickness noise. The agreement was not good for blade passage frequencies, where steady loading noise is probably the primary noise source. The predicted sound pressure levels are slightly overpredicted compared to the measured values, but the trends are the same.

APPENDIX

Definitions of Time Series Formula

Mean Value - The mean value or average is defined by:

$$\mu_x = \lim_{T\to\infty} \frac{1}{T} \int_0^T x(t)dt \tag{1}$$

The typical units are volts.

Mean Square Value - The mean square value is defined by:

$$\Psi_x^2 = \lim_{T\to\infty} \frac{1}{T} \int_0^T x^2(t)dt \tag{2}$$

The typical units are (volts)^2.

Variance - The variance is defined by:

$$\sigma_x^2 = \Psi^2 - \mu^2 \tag{3}$$

The typical units are (volts)^2.

Autocorrelation - The autocorrelation relates how similar a signal is to itself when it is compared at different delay times. It is defined by:

$$\begin{aligned} R_{xx}(\tau) &= \lim_{T\to\infty} \frac{1}{T} \int_0^T x(t)x(t+\tau)dt \\ &= \overline{x(t)x(t+\tau)} \end{aligned} \tag{4}$$

The typical units are (volts)^2. The autocorrelation for a zero time delay is equal to the mean square, $R_{xx}(0) = \Psi_x^2$.

Cross Correlation - The cross correlation relates how similar two signals are. It expresses that relationship at both the same point in time as well as at different delay times. It is defined by:

$$R_{xy}(\tau) = \lim_{T\to\infty} \frac{1}{T} \int_0^T x(t)y(t+\tau)dt \tag{5}$$

The typical units are (volts)^2. The cross correlation is equal to the autocorrelation when both signals are the same.

Power Spectral Density - The power spectral density describes how the energy in the signal is distributed in the frequency domain. It is defined by:

$$\begin{aligned} G_{xx}(f) &= 2\int_{-\infty}^{\infty} R_{xx}(\tau)e^{-j2\pi f\tau}d\tau \\ &= 4\int_0^{\infty} R_{xx}(\tau)\cos(2\pi f\tau)d\tau \end{aligned} \tag{6}$$

The typical units are (volts)^2 sec. The integral of the power spectrum over any given frequency interval is equal to the mean square in that same integral:

$$\Psi_x^2(f_1, f_2) = \int_{f_1}^{f_2} G_{xx}(f)df \tag{7}$$

Cross Spectral Density - The cross spectral density describes how the energy in the cross product of two signals is distributed in the frequency domain. It is defined by:

$$G_{xy}(f) = 2\int_{-\infty}^{\infty} R_{xy}(\tau)e^{-j2\pi f\tau}d\tau \tag{8}$$

The typical units are (volts)^2 sec.

REFERENCES

[1] Sofrin, T. G. and McCann, J. C.: *Pratt and Whitney Experience in Compressor Noise Reduction*, Paper presented at the 72nd Meeting of the Acoustical Society of America, Los Angles, CA., Nov. 2-5, 1966.

[2] Hanson, D. B.: *Spectrum of Rotor Noise Caused by Atmospheric Turbulence*, J. Acoustical Soc. Amer., Vol. 56, No. 1, July 1974, pp. 110–126.

[3] Paterson, R. W. and Amiet R. K.: *Noise of a Model Helicopter Rotor Due to Ingestion of Turbulence*, NASA CR–3213, November 1979.

[4] Simonich, J. C., Amiet, R. K., Schlinker, R. H., and Greitzer, *E. M.: Helicopter Rotor Noise Due to Ingestion of Atmospheric Turbulence*, NASA CR–3973, May 1986.

[5] Paterson, R. W., Vogt, P. G. and Foley, W. M.: *Design and Development of the United Aircraft Research Laboratories Acoustic Research Tunnel*, J. Aircraft, Vol. 10, No. 7, 1973, pp. 427–433.

[6] Hama, F. R.: *An Efficient Tripping Device*, J. of Aeronautical Sciences, Vol. 24, pp. 236-237, March 1957.

[7] Schlinker, R. H. and Amiet, R. K.: *Rotor–Vortex Interaction Noise*, NASA CR–3744, October 1983.

[8] Simonich, J. C.: *Noise Produced by Turbulent Flow into a Rotor: Theory Manual for Atmospheric Turbulence Prediction and Mean Flow and Turbulence Contraction Prediction*, NASA CR-181789, June 1989.

[9] Amiet, R. K.: *Noise Produced by Turbulent Flow Into a Rotor: Theory Manual for Noise Calculation*, NASA CR-181788, June 1989.

[10] Simonich, J. C. and Caplin, B.: *Noise Produced by Turbulent Flow into a Rotor: Users Manual for Atmospheric Turbulence Prediction and Mean Flow and Turbulence Contraction Prediction*, NASA CR-181791, June 1989.

[11] Amiet, R. K., Egolf C. G. and Simonich, J. C.: *Noise Produced by Turbulent Flow Into a Rotor: User Manual for Noise Calculation*, NASA CR-181790, June 1989.

[12] Ribner, H. S. and M. Tucker, *Spectrum of Turbulence in a Contracting Stream*, NACA Technical Report 1113, 1953.

NASA
National Aeronautics and Space Administration

Report Documentation Page

1. Report No.	2. Government Accession No.	3. Recipient's Catalog No.
NASA CR-181792		

4. Title and Subtitle	5. Report Date
Experimental Assessment of Helicopter Rotor Turbulence Ingestion Noise in Hover	June 1989
	6. Performing Organization Code

7. Author(s)	8. Performing Organization Report No.
J. C. Simonich, R. H. Schlinker, and R.K. Amiet	
	10. Work Unit No. 505-63-51

9. Performing Organization Name and Address	11. Contract or Grant No.
United Technologies Research Center East Hartford, CT 06108	NAS1-17763
	13. Type of Report and Period Covered
12. Sponsoring Agency Name and Address	Contractor Report
National Aeronautics and Space Administration Langley Research Center Hampton, VA 23665-5225	14. Sponsoring Agency Code

15. Supplementary Notes

Langley Technical Monitor: Thomas F. Brooks
Final Report

16. Abstract

An experiment was conducted to assess the accuracy of a theory for non-isotropic turbulence ingestion. In order to generate non-isotropic turbulence in a controlled environment, a scale model rotor in a closed chamber was used so that the turbulence generated by the rotor was reingested by the recirculating flow. Simultaneous measurements of turbulence inflow properties and far field acoustics were acquired.

Measurements confirmed that the inflow turbulence was highly non-isotropic. The measured aerodynamic properties were used as inputs for the noise prediction procedure. The general agreement between the non-isotropic noise prediction procedure and the experiment was good, although the procedure generally overpredicts the quasi-tonal low to mid range frequencies and underpredicts the higher broadband signals. The predicted sound power level as a function of polar angle was in close agreement with measurements, except near the rotor plane, which is not modeled by the present analysis. It was determined that the most sensitive parameter influencing the predicted noise was the turbulence intensity.

17. Key Words (Suggested by Author(s))	18. Distribution Statement
helicopter noise, turbulence ingestion noise, rotor noise	Unclassified - Unlimited Subject Category 71

19. Security Classif. (of this report)	20. Security Classif. (of this page)	21. No. of pages	22. Price
Unclassified	Unclassified	67	A04

NASA FORM 1626 OCT 86